

*First name, Name:*  
François Thierry  
  
*Pedagogical accountant for  
the UTT:*  
Christophe Couteau

*Major:* MTE/ONT  
  
*Year:* 2011/2012  
  
*Semester:* Spring 2012

## Foundations of Quantum Mechanics with Single Photons from Quantum Dots

This Master thesis took place in the Photonics Group of the Experimental Physics Faculty of University Innsbruck in Austria.

The study consisted of the realization of a triple slit quantum experiment. The goal was to test the domain of validity of Born's rule upon which relies quantum mechanics. For that purpose we build an heralded single-photon source, implemented data acquisition hard- and software, processed data, created mechanical and electronic components for the apparatus, programmed simulations and worked out theoretical descriptions for part of the physical phenomena involved in the experiment.

*Company:*  
Photonics Department  
Experimental Physics faculty  
University Innsbruck

*Place:*  
Innsbruck, Austria

*Internship director:*  
Gregor Weihs

*Key words:*

- Recherche fondamentale
- 14 Services non marchands
- Optique
- Logiciels - Recherche

## Acknowledgements

I would like to thank all the people who work at the photonics group from the experimental physics department of the University of Innsbruck who made me feel part of the team. I am particularly grateful to Gregor Weihs for giving me the opportunity to come work here and to all the co-workers who were always there for me and gave me all those advices and tips which made my stay so much easier.

I would like to thank especially Stephanie Grabher for teaching me bits of Tyrolean and for helping me with the construction of the source, Benedikt Pressl for his advices on computer matter, Tobias Huber, Patrick Mai, Anna Predojevic and Zoltán Vörös for counselling me when I encountered difficulties, Carina Oberhöler for all the administrative explanations, Thomas Günthner for the life after work, Daniel Föger, Benedikt Pressl and Mathias Sassermann for being good desk room-mates, and all the others I have not named for all kind of reasons

Thanks to all of them for the great ambiance at work, for the kicker play every noon and for all those little things which make it special to work here at Innsbruck.

I can find for each of them several reasons for me to be thankful, and that is what I am really thankful of.

DANKE !

# Contents

<b>Acknowledgements</b>	<b>1</b>
<b>Introducing The University of Innsbruck</b>	<b>4</b>
<b>Introduction</b>	<b>5</b>
<b>1 Context and theory</b>	<b>6</b>
1.1 History and importance of the Born's rule . . . . .	6
1.2 Second order non-linear optics . . . . .	10
1.2.1 Second harmonic generation and spontaneous parametric down conversion . . . . .	10
1.2.2 Phase matching . . . . .	12
1.3 Boyd & Kleinman factor . . . . .	14
1.4 Quantum dots . . . . .	17
<b>2 Experimental set-up</b>	<b>20</b>
2.1 SPDC system . . . . .	20
2.1.1 Temperature controller . . . . .	21
2.1.2 Heralded single-photons source . . . . .	21
2.1.3 Coincidences counter . . . . .	28
2.1.4 Characterization of the source . . . . .	29
2.2 Quantum dot source . . . . .	31
2.3 Three path set-up . . . . .	32
2.4 Slits systems . . . . .	34
2.4.1 System used . . . . .	34
2.4.2 The new designs . . . . .	35
2.4.3 Motor driver circuit . . . . .	36
2.4.4 Testing the new systems . . . . .	38
<b>3 Results</b>	<b>40</b>
3.1 Laser . . . . .	40
3.2 Heralded Single-Photons Source . . . . .	43
3.3 Quantum dot . . . . .	44
3.4 Quaternion criterion . . . . .	46
<b>Summary</b>	<b>48</b>
<b>Bibliography</b>	<b>48</b>
<b>A Results</b>	<b>52</b>
A.1 Laser . . . . .	52
A.2 Heralded single-photon source . . . . .	53
A.3 Quantum dot source . . . . .	54
<b>B Python codes</b>	<b>55</b>
B.1 Two lenses ABCD system . . . . .	55
B.2 Shatter system test . . . . .	56
B.3 Analyze data from measurements . . . . .	58

<b>C Electronics schematics</b>	<b>61</b>
C.1 Coincidence circuit . . . . .	61
C.2 Stepper motors driver circuit . . . . .	62

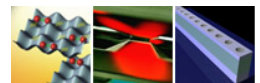
# Introducing The University of Innsbruck

## University of Innsbruck

The University of Innsbruck is one of oldest universities of Austria. Founded in 1669, it currently employs over 4 000 staff for over 27 000 students making it western Austria's largest institution. Located in the Alps, its 15 faculties cover all fields of research and education. The University collaborates with numerous international research and education institution in order to provide an international exchange in research and teaching.



## Institute for Experimental Physics



The Institute for Experimental Physics is part of the Faculty of Mathematics, Computer Science and Physics which provides excellent research in combination with an attractive teaching resulting from a close relationship between its specialities. The institute conducts experimental research in many area of physics, in particular quantum information, spectroscopy, quantum optics, cold atoms, quantum gases, solid state physics, and photonics. The institute currently employs 86 people including the students that are currently conducting research.

## Photonics Group

The Photonics Group is led by Prof. Gregor Weihs and conducts research in quantum optics, nonlinear optics, optics of semiconductor nanostructures, and in addition performs experiments on the foundations of quantum physics. This Group currently has 16 staff.



Gregor Weihs



People currently working at the photonics group  
(Lorenz Butschek, Lukas Einkemmer and Daniel Föger are not represented here)

# Introduction

*"To present a scientific subject in an attractive and stimulating manner is an artistic task, similar to that of a novelist or even a dramatic writer. The same holds for writing textbooks."*  
Max Born *My Life & My Views* (1968)

One of the most successful experiments in quantum mechanics is certainly the double-slit experiment conducted by Thomas Young in 1903 [1] which proved the wave-particle duality of light. This experiment was extended to electrons by Claus Jönsson in 1961 [2] who showed that, as predicted by theory, interference of two possible paths exist. Other paths experiments with more than two paths were conducted and were described according to the Born's rule. The Born's rule gives the probability  $P(r, t) = |\psi(r, t)|^2$  to find a particle in a particular unit of volume. That allows us to follow the propagation of such quantum particles. Deriving this rule shows that a possible test can come from the fact that quantum interferences from three or more paths can always be described as a sum of the effects from double-slit experiments, that is there is no third or higher order interference [3]. A deviation from this statement would lead to reconsider the probabilistic interpretation of quantum mechanics and therefore lead to a more inconvenient formulation of this theory [4].

The Young's slit experiment was extensively studied and became a world-wide used practical example to show students effect of quantum mechanics and help them understand the uncertainty principle. The Born's rule was taken for granted but it is only very recently that this prediction was matched for three-slits experiment within error margin of 1% [5], and for three-paths experiment within error margin of 0.2% [6]. Authors of those papers predicted that this bound can again be reduced by orders of magnitude with more control over the count rate of the detector in the experiment which seemed to be the major limitation in terms of error.

The purpose of this report is to present a three-path experiment using single photons sources. The sources are a heralded single-photon source which uses a second order non-linear effect called parametric down conversion to produce pairs of correlated photons and a source based upon single-photons emission coming from the relaxation of InAs quantum dots embedded in a GaAs substrate. The expected result is that by using single photons, one will have good control over the count rate of the detector and therefore will reduce the limit of validity of Born's rule and quantum mechanics in general.

In a first part I will introduce the Born's rule and its importance as well as the theory behind paths experiments and parametric down conversion. The theory behind the quantum dots emission will also be briefly describe. An intriguing calculus will also be discussed concerning the optimization of second order non-linear effects. Secondly I will present the entire set-up (components, hard- and software). Then I will describe the results and possible improvements of the experiment. Finally I will conclude on the success of the study and present some possible ways of extending the testing of this rule.

# 1 Context and theory

## 1.1 History and importance of the Born's rule

Quantum mechanics is a branch of physics that deals with discrete, indivisible units of energy called quanta. Since it has been discovered in the early 20th century it has revolutionized our way of understanding many topics, explained many phenomena from the tiniest scale to the biggest one and led to numerous technological advances. It relies solely upon four main ideas:

- Energy is not continuous but comes in small and discrete units
- Particles behave like particles and like waves both in the same time
- The movement of those particles is inherently random, following probabilities
- It is impossible to know both the position and momentum of a particle (the more precisely one is known the less we know about the other)

Born's interpretation of probability that he defined in his two papers from 1926 [7] [8], is one of the key principle of quantum mechanics. Foundation of quantum theory who took place between 1900 and 1927 can indeed be defined singly within a few papers [9].

Quantum physics began with Planck's publication on the discovery of quantum theory (1900), then came Einstein on the notion of quanta (1905) followed by Bohr's description of the hydrogen atom (1913) and the introduction of statistics by Bose (1924). Thanks to the introduction of statistics the interpretation of quantum mechanics began to change and so did formulations. Schrödinger used matrix mechanics (1925) and Heisenberg presented a paper on wave mechanics (1926). Finally three persons closed this birth period of quantum mechanics. It started with Heisenberg asking for the inclusion of the notion of observables (1925), continued with Born's remarks on probability and causality (1926) and finished with Heisenberg's uncertainty relations and Bohr's formulation of complementarity (1927).

Born's remark from 1926 states beautifully the essence of wave mechanics as we know it and bring the essence of the test conducted in this thesis:

"The motion of particles follows probability laws but the probability itself propagates according to the law of causality."

For having developed this statistical interpretation of quantum states, Max Born was attributed a Nobel Prize in 1954. According to his description in term of probabilities over Schrödinger's wave function  $\psi(r, t)$  [10], the motion of a particle or the probability  $P(r, t)$  for this particle to be in a certain volume  $d^3r$  in a position  $r$  at a time  $t$  is described as in equation 1.1. The normalized wave function  $\psi$  is often referred as probability amplitude which has a probability density  $P$ . What Born really did was to give a physical meaning to the wave function. Before him the properties of  $\psi$  were used to make some predictions in the young field of atomic physics (atoms emitting at discrete energies...) but  $\psi$  was not really linked to any physical description.

$$P(r, t) = \psi^*(r, t)\psi(r, t)d^3r = |\psi(r, t)|^2d^3r \quad (1.1)$$

To better understand how this interpretation works let us suppose that a quantum system is in a state  $|\psi\rangle$  and that we want to measure an observable  $\hat{A}$  of the system.  $\hat{A}$  can be the energy, the position or the spin of the system at a given time. Observables such as  $\hat{A}$  can be described using eigenvectors which can be seen as unit vectors in a plane for the observable.

These eigenvectors can be multiplied by the eigenvalues to find  $\hat{A}$ . If one or more eigenvalues are the same they are considered degenerate and bring an additional complexity to the resolution of the system as they are more complicated to define singly. The eigenvectors of  $\hat{A}$  are noted  $|a_i\rangle$  and the corresponding eigenvalues  $\alpha_i$ , that we suppose non-degenerate to simplify. As postulates the principle of reduction of the wave packet which states that a system in a superposition of states reduces to only one state when studied by an observer, the measure of  $\hat{A}$  can give only one result of  $\alpha_i$ , and the probability to obtain this result is  $|\langle a_i|\psi\rangle|^2$ . Let us suppose that the measure gives  $\alpha_p$  for a result, the system passed in immediately during the measure from the indefinite state  $|\psi\rangle$  which can be a superposition of several states to the state  $|a_p\rangle$ .

We then can see the use that we can make of scalar products  $\langle a|\psi\rangle$ , where the system  $|a\rangle$  is in any state. By supposing the existence of an observable of  $|a\rangle$  which would be one of the eigenstate, we can say that the probability to find the system in the state  $|a\rangle$  (i.e. if we measure in which state the system is) is  $|\langle a|\psi\rangle|^2$ . This is why the scalar product is called probability amplitude and this formulation, thanks to the scalar product algebraic properties, greatly simplify quantum computations.

A way of describing the three-slits experiment while testing the Born's rule was established by R.D. Sorkin [3] [11]. It starts from Born's statistical interpretation of the Shrödinger's wave function  $\psi(r, t)$  (eq. 1.1) which gives the probability for a quantum system under measurement to give a certain result when we look at the position observable.

$$P(r, t) = \psi^*(r, t)\psi(r, t) = |\psi(r, t)|^2 \quad (1.2)$$

Sorkin introduced interference terms of exclusive slits (i.e. paths or events  $A, B, C, \dots$ ) deriving from the classical additivity of the probabilities also known as sum rule. This approach, also called sum over histories can describe many-paths systems like a classical probability theory.

The sum rule was established by Kolmogarov in 1931 [12]. Equation 1.3 gives the formulation of this rule for two mutually non exclusive events. It states that the probability for a system involving two events to give a certain output is the sum of the probabilities for both events to happen minus the probability that both events happens simultaneously.

$$P(A \cup B) = P(A) + P(B) - P(A \cap B) = 1 \quad (1.3)$$

In classical mechanics  $P(A \cap B) = 0$ , as an example, a rolling dice will only give one result which is the probability for an event (a number facing up) to happen but it is not possible for two events to happen simultaneously as in quantum mechanics where  $P(A \cap B) \neq 0$ .

According to Sorkin's interference terms, the three orders of interference, which describes a three paths system are given in equation 1.4. They come directly from the sum rule,  $I_{x, \dots, x_n}^n = P(x \cup \dots \cup x_n)$  and  $P_{x, \dots, x_n} = P(x \cap \dots \cap x_n)$  and describe non exclusive events.

$$\begin{aligned} I_A^0 &= P_A \\ I_{AB}^1 &= P_{AB} - P_A - P_B \\ I_{ABC}^2 &= P_{ABC} - P_{AB} - P_{AC} - P_{BC} + P_A + P_B + P_C \end{aligned} \quad (1.4)$$

Here  $I_A^0$  describes the zeroth order of interference when only the path  $A$  is open, as expected it is equal to  $P_A$  which is the probability for a particle to be detected in the detector associated with the path  $A$ .

Now let's consider the first order of interference  $I_{AB}^1$ . For classical particules it is equal to zero as there is no interference. There is no interference because the probability  $P_{AB}$  will just be the sum of the probabilities for a particle of travelling through the path  $A$  or the path  $B$ , in fact this classical particle can only go in one path at the time so the detection counts after the system when dealing with the same amount of particles will be the same.

Therefore in the classical case  $P_{AB} = P_A + P_B$  for the two paths simultaneously open or for one and then the other open, and therefore  $I_{AB}^1 = 0$ . This however does not describe quantum particles and classical waves which can interfere because their amplitudes are modulated in time. For these particles the first order of interference is violated,  $I_{AB}^1 \neq 0$  which means that  $P_{AB} \neq P_A + P_B$  and that the situation two paths open is no longer the same as the one where one is opened after the other, two-path interference appears.

But according to Born's remark of 1926 the second order must hold. From this interpretation the probability density must follow the classical Kolmogorov sum rule so that every three or more paths system is just a combination of two and one path as  $P_{ABC} = P_{AB} + P_{BC} + P_{CA} - P_A - P_B - P_C$  will fulfill the condition  $I_{ABC}^2 = 0$ . The formulation of  $P_{ABC}$  comes directly from equation 1.2 this is why a violation of the second order of interference will lead to a reformulation of quantum mechanics. Therefore the error in Born's rule validation measurements is directly related to quantum mechanics validity and reducing this error will reassure the use of this theory.

In order to test Born's rule and the probabilistic interpretation of the wave function one can verify that there is no second order interference for three-path set-up, that  $I_{ABC}^2 = 0$ . One of the ways for us to measure this effect and experimentally prove the rule is by splitting a beam in parts which will go in different paths either opened or closed in a way that we can probe the second order of interference by collecting the intensities or counts rate on a detector, and that for each slit configuration to evaluate every term of  $I_{ABC}^2$ . We model an experimental second order interference  $I_{ABC}^2$  quantity to probe by defining:

$$\begin{aligned}\epsilon &= I_{ABC}^2 - P_0 \\ &= P_{ABC} - P_{AB} - P_{AC} - P_{BC} + P_A + P_B + P_C - P_0\end{aligned}\quad (1.5)$$

Where  $P_0$  is the experimental background due to dark counts and scattered light as it can be no zero detection even when all the paths are closed. Minimizing  $P_0$  will lead to a better test of the rule and bring  $\epsilon$  closest to zero as expected by the theory. That is why all experimental errors have to be tracked down in order to compensate them. Then to exacerbate the effect we normalize  $\epsilon$  over  $\delta$ , the expected first order interference. This gives the ratio of the violation of the second order interference over the the expected violation of the first order. The measurement of this normalization that is called  $\kappa$  will indicate the degree of validity of the Born's rule and the minimization of this measure is the subject of this study.

$$\begin{aligned}\delta &= |I_{AB}| + |I_{BC}| + |I_{CA}| \\ &= |P_{AB} - P_A - P_B + P_0| + |P_{BC} - P_B - P_C + P_0| + |P_{CA} - P_C - P_A + P_0|\end{aligned}\quad (1.6)$$

$$\kappa = \frac{\epsilon}{\delta} \quad (1.7)$$

To measure  $\kappa$  we have to measure all single- and two-paths terms. So we have to evaluate all of the terms of equation 1.5. To do that we build a set-up where three (up to five in the latest designs) shatters can be independently closed or opened. As we try to narrow down the margin of error over an expected null value, any experimental error or fluctuation will directly impact the accuracy of our results. This is why all components of the set-up must be carefully studied to remove as possible those deviations.

As we measure intensities or photons counts, a special attention will be given on both ends of the system, meaning source and detector. The main source of error from the detector is its acquisition speed. Because the detector cannot register events continuously it misses some of the photons leading to deviations over several acquisition, this is called detector non-linearity. This non-linearity from the detector can be estimated and compensated using detector dead time and background count rate which need to be precisely determined. More detailed information on compensating detector non-linearity for our three-paths interferometer can be found in [6].

Fluctuation in intensities may also come from the fact that the power of a laser source is never perfectly stable. In order to minimize this effect a measurement of the power in parallel to the proper paths experiment would allow the possibility to remove the fluctuations by subtracting this signal from the kappa measure and therefore narrow down the precision. Another fluctuation can come from the fact that the temperature fluctuates inside the laboratory room and therefore introduce changes of lengths in the interferometer (optical components dilatation). This effect is compensated by correcting the phase of the beams in the three-paths interferometer while measuring in order to find the maximum of intensity for the interference.

To go further on those limitations it was proposed to use single photon sources to be able to know the number of photon emitted and to set the emission rate to have as little photons arriving at the detector during its dead time as possible. Such a source will solve both problems as there will be no more fluctuations of the output power (or we know the fluctuations because we know how many were emitted) and it will also reduce the detector non-linearity. This is why this study will use two different single-photon sources, an heralded single-photon source generated by spontaneous parametric down-conversion of a laser beam in a non-linear crystal, and a source from quantum dots emission.

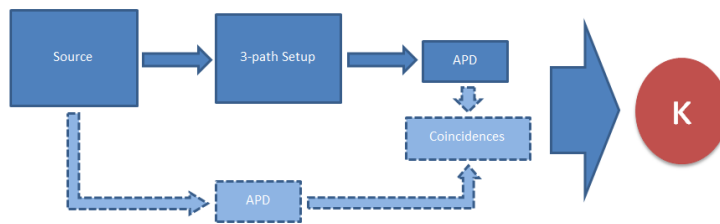


Figure 1.1: Principe schématisé du déroulement de l'expérience  
(En pointillés les composants propres à la source de photons corrélés)

Another interesting approach for the experiment was described by A. Peres in his paper from 1979 [13] where he describes an experiment with three-scatterers interference and tries to search for quaternionic effects in quantum mechanics. As scatterers can be seen as making take three different paths to an incident beam it is a kind of paths experiment. As its formalism is close to ours, it would be interesting to test further quantum theory while testing Born's rule.

Discovered in 1843 by Hamilton [14] for use in mechanics in 3D-space quaternions have the form  $a + ib + jc + kd$  with  $i^2 = j^2 = k^2 = ijk = -1$ . As Hurwitz proved in 1898 [15] that normed composition algebras where  $|xy| = |x||y|$  can only be of dimension 1 (real), 2 (complex), 4 (quaternion) and 8 (octonion), they can be described by vectors in a 4D-plane and directly extend the complex system which take the form  $a + ib$  and represent vectors in a two dimensionnal space.

Peres uses the scattering amplitude  $P_A = |\langle a|\psi \rangle|^2$  to represent what is coming on the plane of detection of the detector for particles scattered by the scatterer  $A$  (i.e detection of particles who took the path  $A$ ). The scalar product  $\langle a|\psi \rangle$  can be expressed as in equation 1.8 for complex algebra or uni-modular quaternion and therefore according to the superposition principle which states that the result of an event involving two variables is the sum of the effects of the variables, the probability for an event to be detected for two scaterers present is  $P_{AB}$  as stated in equation 1.9.

$$P_A = |\langle a|\psi \rangle|^2 \quad (1.8)$$

$$\langle a|\psi \rangle = a \exp(i\phi_a)$$

$$P_{AB} = P_A + P_B + 2\sqrt{P_A P_B} \cos(\phi_A - \phi_B) \quad (1.9)$$

Peres proposed to study the cosines  $\alpha, \beta$  and  $\gamma$  of the phase differences between the paths pairwise that according to our formalism can be described as equations 1.10 respectively.

Those cosines should be equal to  $\pm 1$  for real algebra as it is trivial to see that in this case  $P_A = a^2$ ,  $P_{AB} - P_A - P_B = \pm 2ab$  and  $\alpha = \pm 2ab/\pm 2ab$ . It should stay  $< 1$  if the algebra is complex or quaternionic because in this case  $\alpha = \frac{2ab\cos(\phi_a)\cos(\phi_b)\cos(\phi_a - \phi_b)}{2ab\cos(\phi_a)\cos(\phi_b)} = \cos(\phi_a - \phi_b)$  which is contained between 0 and 1. If they are  $> 1$  the superposition principle is violated and as seen before the sum rule does not apply anymore. Peres defined a criterion  $F(\alpha, \beta, \gamma)$  to determine the algebraic nature of quantum theory (equation 1.11).

$$\alpha = \frac{P_{AB} - P_A - P_B}{2\sqrt{P_A P_B}} \quad \beta = \frac{P_{BC} - P_B - P_C}{2\sqrt{P_B P_C}} \quad \gamma = \frac{P_{AC} - P_A - P_C}{2\sqrt{P_A P_C}} \quad (1.10)$$

$$F(\alpha, \beta, \gamma) = \alpha^2 + \beta^2 + \gamma^2 - 2\alpha\beta\gamma \quad (1.11)$$

If  $F(\alpha, \beta, \gamma) = 1$  complex algebraic nature can be assumed because  $\alpha, \beta$  and  $\gamma$  are not independent as the angles sum up to zero. Another way to see it is to admit that as these angles sum up to zero, they are all in the same plane, the detection plane. But for quaternions that do not behave like vectors in a plane but as vectors in a 4D-space it is impossible to define a detection plane that would detect all constituents. Therefore  $0 < F(\alpha, \beta, \gamma) < 1$  and the algebra contain some quaternionic components. Again, if  $F(\alpha, \beta, \gamma) > 1$  the superposition principle is violated.

While testing the Born's rule one can also try to test the algebra of quantum mechanics theory to see if it is complex or quaternionic and in this thesis we will also present the results of the criterion proposed by Peres for our three-paths experiment.

## 1.2 Second order non-linear optics

Since the invention of laser in 1960 non-linear optics has been of interest. As observations conflicted with previous assumptions concerning light passing through a non-linear optical medium, it was verified experimentally that the refractive index in such medium depends on the light intensity, the optical frequency can change and the superposition principle is violated, it becomes a non-linear effect [16] where the response of a system to two excitations is no longer the sum of the effects of these excitations. Taking advantage of such phenomena led to an abundance of applications with frequency conversion systems as one example.

There are some domains of the electromagnetic spectrum where laser diodes are difficult to manufacture. Diodes in the yellow and orange wavelength ranges cannot be produced due to a lack of materials with the corresponding band gap to emit at these wavelengths. Wavelengths lower than 370 nm are currently not possible to achieve due to fabrication technique limitations. Diodes in the blue wavelength range are not diversified due to a lack of consumer demand which controls the development of products in this sector. Indeed while the market for red and infra-red diodes is large and the Blu-ray technology increased the demand for diodes at 405 nm, the selection of blue wavelengths is still limited. This is why frequency conversions systems take a special importance in today optics as they can supply coherent light at wavelengths that cannot be generated easily using laser diodes.

### 1.2.1 Second harmonic generation and spontaneous parametric down conversion

Second harmonic generation (SHG), also called frequency doubling is a non-linear effect produced when an electromagnetic wave of a certain frequency passes through a  $\chi^{(2)}$  non-linear crystal. The photons are pairwise combined to form new photons with twice the energy. The light at the output of the crystal is a mixture of the two waves, the incoming and the produced one. By filtering it to suppress the pump wave one can therefore produce a light doubled in frequency after passing in a second order non-linear material.

Spontaneous parametric down-conversion (SPDC) which is sometimes also called parametric fluorescence or parametric scattering in older papers is also a second-order non-linear effect. In fact it is the inverse process of SHG where a photon is split in two half energetic ones. SPDC is also the initial process leading to optical parametric oscillators where the crystal is placed inside of a cavity to amplify the output beam much like a laser cavity does. It generates the first photons upon which the coherent output is built by parametric amplification. Parametric oscillators have a large frequency tuning range and are typically used as source of tunable, narrowband excitation light in fields ranging from spectroscopy to quantum optics. SPDC is also a process of choice to produce entangled pairs of photons.

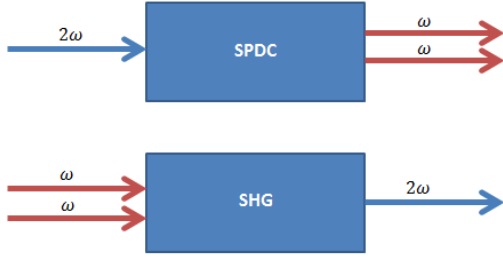


Figure 1.2: Principe de fonctionnement des processus SPDC et SHG

During SHG the interaction of an electromagnetic field of angular frequency  $\omega_1$  with a  $\chi^{(2)}$  non-linear crystal will produce a response  $\omega_2 = 2\omega_1$ . This effect has to respect the fundamental laws of energy conservation  $\hbar\omega_2 = 2\hbar\omega_1$  and momentum conservation  $\hbar k_{2\omega} = 2\hbar k_\omega$ . During SPDC one high frequency photon spontaneously splits into two lower frequency photons such that energy is conserved, the conservation laws still remain. This set some constraints on frequency matching and phase matching conditions as we will see later.

SPDC and SHG are two symmetrical effects and are described using the same formalism. The main difference between SHG and SPDC is that for SPDC the distribution of generated photons depends on the input power, at low input power the converted photons are thermally distributed but at high power they follow the same poissonian distribution as for SHG at any power [17]. We used both effects in our source, here we present only the formalism for SHG as it is more studied because it produces coherent light in the blue domain where there is a lack of laser diodes but the same formalism can be applied to SPDC.

The coupled wave equations describing the frequency doubling are defined as:

$$\begin{aligned} \frac{dA_{2\omega}}{dz} &= i\Gamma A_\omega^2 e^{-i\Delta kz} \\ \frac{dA_\omega}{dz} &= i\Gamma A_{2\omega} A_\omega^* e^{-i\Delta kz} \end{aligned} \quad (1.12)$$

With  $A_l = \sqrt{\frac{n(\omega_l)}{\omega_l}} E_l$  the normalized amplitude and  $\Gamma = \frac{2d_{eff}}{c} \sqrt{\frac{\omega^3}{n_{2\omega} n_\omega^2}}$  the coupling coefficient [18].

The solutions to those wave equations are formulated in two regimes, the weak and strong conversion regime. Here we will only consider the weak conversion regime. The weak conversion regime describes a situation where the generated wave radiating at the doubled frequency does not significantly diminish the pump (fundamental) wave. Therefore, only the first equation of 1.12 plays a role. To solve this problem for the interaction of electromagnetic waves in a crystal with length  $L_c$ , a simple integration leads to the result:

$$A_{2\omega} = \Gamma L_c A_\omega^2 e^{\frac{i\Delta k L_c}{2}} \text{sinc}\left(\frac{\Delta k L_c}{2}\right) \quad (1.13)$$

As the intensity is proportional to the square of the normalized amplitude  $I \propto |A|^2$ , it varies as the square of the crystal length. Therefore the behaviour of the phase mismatch is contained in the argument of the *sinc* term which is sometimes called the phase matching function and characterize the effect of tuning the phase matching over the conversion efficiency [17]. From the condition  $\text{sinc}(\Delta k L_c/2) = 0$  the so-called coherence length  $l_c$  can be defined. This is the length at which a phase shift of  $\pi$  is introduced, corresponding to the "half period of the growth and decay cycle of the second harmonic" [19].

$$l_c = \frac{\pi}{\Delta k} = \frac{\lambda}{4(n_{2\omega} n_\omega)} \quad (1.14)$$

It is clear that constant growth of the intensity with crystal length is only possible for perfect phase matching, where  $\Delta k = 0$  for the *sinc* term to be null. That means that we are at the maximum of the growth of the generated wave. That is why the efficiency of the conversion strongly depends on the wave-vector mismatch  $\Delta k$  between the pump and the generated photons.

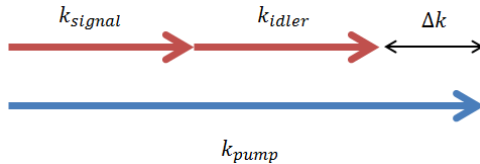


Figure 1.3: Principe de la conservation des moments et de la nécessité de l'accord de phase

### 1.2.2 Phase matching

The condition  $\Delta k = 0$  for the interaction of interest is called phase matching. Physically, it corresponds to the requirement that, in each section of the crystal, the wave locally generated by the non-linear polarization must add up in phase with the waves generated by all other sections of the crystal. Achieving phase matching is one of the central problems of practical non-linear optics [20].

Because of its wavelength dependence, the refractive indices of fundamental and second harmonic waves generally differ  $n_\omega \neq n_{2\omega}$ . Destructive interferences appear between second-harmonic waves that are generated at different locations in the crystal, as they have different phases. So in order to maintain the second order non-linear effect effective, additional procedures have to be applied to keep the relative phase steady. This is phase matching and it can be of two types. In type I phase matching the two photons in the non-linear process have to be collinearly polarized (i.e. have the same polarization), in the type II the two photons are orthogonally polarized. Our source uses type II phase matching.

Several methods exist to achieve it, each one having advantages and disadvantages. The two main common methods used are birefringent phase matching techniques (PM) and quasi-phase matching (QPM) techniques. Birefringent phase matching tries to manipulate the difference in refractive indices of fundamental and second-harmonic wave by means of the birefringence that occurs in different media. Quasi-phase matching reverses the sign of the non-linear susceptibility with a certain periodicity. Other methods exist even though they are less often used. In this study we will only develop the QPM method as it is the method used in the SPDC source we build.

As for phase matching, angle and temperature tuning are needed to establish second harmonic generation for the wavelength at hand. Formulas to derive tolerances for wavelength (eq. 1.15), temperature (eq. 1.16) and for angle (eq. 1.17) are given in general terms and specifically for PPKTP (periodically poled potassium titanyl phosphate  $\text{KTiOPO}_4$ ) the crystal we used in [21]:

$$\Delta\lambda = \left| \frac{1.39\lambda}{\pi L_c \left[ \frac{1}{2} \frac{dn_{2\omega}}{d(\lambda/2)} - \frac{dn_\omega}{d\lambda} - \frac{n_{2\omega} - n_\omega}{\lambda} \right]} \right| \quad (1.15)$$

$$\Delta T = \left| \frac{1.39\lambda}{\pi L_c \left[ \left( \frac{dn_{2\omega}}{dT} - \frac{dn_\omega}{dT} \right) - \alpha(n_{2\omega} - n_\omega) \right]} \right| \quad (1.16)$$

$$\Delta\theta = 1.883 \sqrt{\frac{n_{2\omega}}{n_\omega} \frac{\Lambda}{L_c}} \quad (1.17)$$

$$n_z^2 = 2.3136 + \frac{1.00012}{1 - 0.05679\lambda^{-2}} - 0.01679\lambda^2 \quad (1.18)$$

The refractive indices experienced by the two beams can be calculated using Sellmeier coefficients in order to evaluate these tolerances. These coefficient were calculated for hydrothermal KTP by Vanherzeele et al. in 1988 [22], in our case we used the refractive index along the  $z$  axis (eq. 1.18). In addition one can perform angle tuning which is a critical phase matching or temperature tuning if one wants to perform a non critical phase matching and also look at other tolerance functions that one can use to take into account some imperfections of the crystal [21].

But phase matching is not the only parameter upon which one can perform conversion efficiency improvements. The other important parameters that one as to keep in mind while conducting experiments with second order non-linear effects are mainly inherent to the crystal used:

- Wavelength transparency range
- Effective non-linear coefficient
- Damage threshold
- Walk-off angle

### Quasi-phase Matching

The concept of quasi-phase matching was first showed by Armstrong and al. in 1962 [23]. QPM does not match the refractive indices to achieve phase matching. It maintains the average relative phase but still enables the second-harmonic intensity to grow.

In contrast to phase matching techniques, in QPM the non-linear susceptibility changes its sign, leading to a change in the spontaneous polarization  $P_S$ . This periodic pattern can be taken into account using a Fourier series to denote the spatially varying non-linear susceptibility.

$$d(z) = d_{eff} \sum_{m=-\infty}^{\infty} (G_m e^{-iK_m z}) \quad (1.19)$$

$$G_m = \frac{2}{m\pi} \sin\left(\frac{m\pi L_c}{\Lambda}\right)$$

The function  $G_m$  represents a Fourier coefficient taking into account the geometric period length,  $\Lambda$ . Inserting the Fourier series into the solution achieved for the coupled wave equations in the second-harmonic case and assuming weak conversion leads to a simplification: only the Fourier component which fulfills the phase matching condition is taken into account while all others contribute weakly. The condition to achieve QPM is met if the phase mismatch  $\Delta k$ , equals the reciprocal domain space vector  $K_m$ , i.e. if there is a phase inversion at the domain edge.

$$\Delta k = K_m = \frac{2\pi m}{\Lambda} \quad (1.20)$$

Hence,  $d(z)$  is reduced to its relevant harmonic,  $d_Q$  which is related to the Fourier component meeting the phase matching condition as equation 1.21. Analyzing the first order QPM effect ( $m = 1$ ) for the optimum condition where  $\sin(\frac{\pi L_c}{\Lambda}) = 1$ , it happens that the effective susceptibility is reduced by a factor of  $2/\pi$  (equation 1.22)

$$d_Q = d_{eff} G_m \quad (1.21)$$

$$d_Q = d_{eff} \frac{2}{\pi} \quad (1.22)$$

The expression for the second-harmonic field generated under these conditions becomes:

$$A_{2\omega} \approx i \frac{\Gamma}{d_{eff}} d_Q L_c A_\omega^2 e^{\frac{i\Delta k L_c}{2}} \text{sinc}(\frac{\Delta k L_c}{2}) \quad (1.23)$$

Propagating through the non-linear crystal, the generated beam intensity will oscillate with a period called the coherence length which is defined by  $l_c = \frac{\pi}{\Delta k}$  as expressed in 1.14. One coherence length is half a period of the growth and decay cycle of the second harmonic, this is why an inversion of the relative phase is forced after an odd number of coherence lengths. Changing the sign of power flow and thereby the relative phase between the incident and generated wave after an odd number of coherence lengths allows the non-linear process to be reset just at the maximum of a growth cycle, this way effective intensity increase can be achieved. If the reversal of power flow takes place every coherence length, the process is called first order QPM. The goal of the QPM is to find a way to reverse the sign of  $d_{eff}$  periodically with  $l_c$  in order to suppress the destructive interference and increase the conversion efficiency.

QPM does not produce second harmonic frequencies as efficiently as proper phase matching, due to slower intensity growth rates as can be seen in Figure 1.4. But it still remains an adequate alternative and allows the prospect of using isotropic media (such as GaAs) and the freedom of polarization choice. The theoretical approach to SGH and SPDC with quasi-phase matching is similar to the case for homogeneous media. Only the basic differences will be pointed out here. [19] can be referred to for a more detailed consideration.

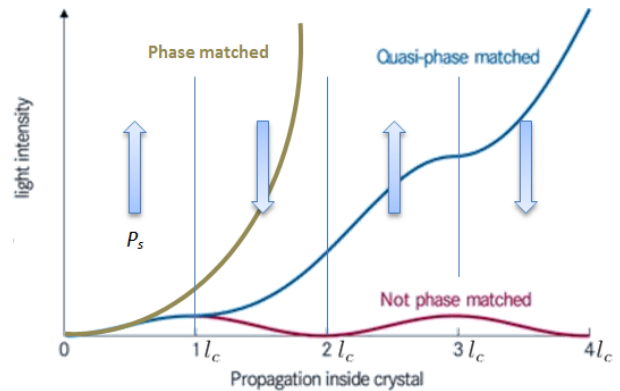


Figure 1.4: Schéma de l'effet de l'accord de phase

### 1.3 Boyd & Kleinman factor

The Boyd & Kleinman theory initially published in 1968 [24] gives the theory behind second harmonic generation, parametric generation and frequency mixing in general. They established a factor to optimize the power of the generated beam, this factor is now widely used when dealing with non linear crystals. According to this factor the power of the generated wave is as it follows:

$$P_{2\omega} = \frac{16\pi^2 d_{eff}^2}{\epsilon_0 c \lambda_\omega^3 n_{2\omega} n_\omega} P_\omega^2 e^{-\alpha' L_c} L_c h(\sigma, \beta, \kappa, \xi, \mu) \quad (1.24)$$

This equation includes  $P_\omega$  the incident power and  $L_c$  the crystal length. The others parameters are  $d_{eff}$  effective susceptibility,  $\epsilon_0$  vacuum permittivity,  $c$  velocity of light,  $\lambda_\omega$  incident wavelength,  $n_{2\omega}$  and  $n_\omega$  refractive indices for the two waves,  $\alpha' = \alpha_\omega - \alpha_{2\omega}$  absorption in the material and of course  $h(\sigma, \beta, \kappa, \xi, \mu)$  the Boyd & Kleinman factor.

As one can see, all parameters are fixed when doing a measurement. A lot of parameters depend on the crystal, others on the incident beam but it is straight forward that the only way for variations within a particular experiment to appear is through this factor. This is this factor, sometimes called focusing factor, which will then determine the quality of the output beam for a specific set-up. This factor can be calculated according to the following definition:

$$h(\sigma, \beta, \kappa, \xi, \mu) = \frac{1}{4\xi} e^{\mu \alpha L_c} \iint_{-\xi(1-\mu)}^{\xi(1+\mu)} \frac{e^{-\kappa(\tau+\tau')} e^{i\sigma(\tau-\tau')} e^{-\beta^2(\tau-\tau')^2}}{(1+i\tau)(1-i\tau')} d\tau d\tau' \quad (1.25)$$

This equation takes as parameters :

$$\text{Phase mismatch } \sigma = \frac{1}{2}b\Delta k$$

$$\text{Birefringence parameter } \beta = \frac{\rho}{\delta_0}$$

$$\text{Absorption factor } \kappa = \frac{1}{2}\alpha b$$

$$\text{Focal strength } f = \frac{L_c}{b}$$

$$\text{Focal position } \mu = \frac{L_c - 2f}{L_c}$$

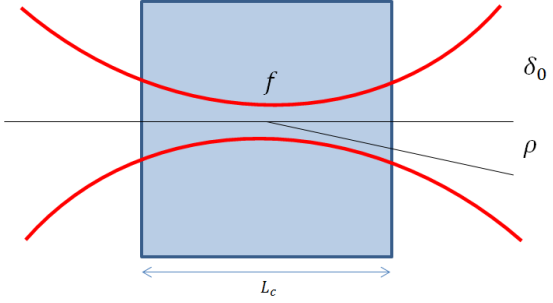


Figure 1.5: Vision très schématique du rayon dans le cristal

Here  $b = \omega_0^2 k_\omega$  is the confocal parameter,  $\delta_0 = \frac{2\omega_0}{b}$  the half angle and  $\Delta k = 2k_\omega - k_{2\omega} = \frac{2\omega_0}{c}(n_\omega - n_{2\omega})$  the phase mismatch between the wave vectors of the two beams.

If one wants to see the effect of focusing or in other words to see how the size of the beam inside the crystal affects the power of the output beam, he has to vary the confocal parameter  $b$ . It can be assumed for simplification that there is no absorption and that the focus position is at the center of the crystal. In that case  $\kappa = \mu = 0$  and we can set  $\beta = B\xi^{-1/2}$  with  $B = \frac{\rho(L_c k_\omega)^{1/2}}{2}$  the walk-off parameter which relies only on fixed values. The optimum focusing factor then becomes  $h_m(B, \xi) = h(\sigma_m(B, \xi), B\xi^{-1/2}, 0, \xi, 0)$  which consists of the following equation:

$$h_m(B, \xi) = \frac{1}{4\xi} \iint_{-\xi}^{\xi} \frac{e^{i\sigma_m(\tau-\tau')} e^{-B^2(\tau-\tau')^2/\xi}}{(1+i\tau)(1-i\tau')} d\tau d\tau' \quad (1.26)$$

By resolving this equation one can obtain the optimum focusing parameter with  $\sigma_m = 0.57$  for a given walk-off  $B$  in function of the focal strength  $\xi$  and therefore in function of  $b$ , the confocal parameter. This gives the "textbook" result of Boyd & Kleinman theory (Figure 1.6).

This function being very computationally demanding there were some attempts [25] [26] to make it more convenient to use in practical applications. Indeed this is of interest because most of today's laser diodes produce elliptical beams that is why a 2D map of this optimum focusing parameter is often needed to quickly evaluate the theoretical output of a particular frequency conversion set-up and determine a given crystal performance. We implemented the approximation of Y.F and Y.C Chen [26]. In their paper they proposed a Lorentzian shaped approximation of the optimal focusing factor as an analytical representation to remove the 2D integral and optimization procedure which are the two most computationally intensive parts of equation 1.26.

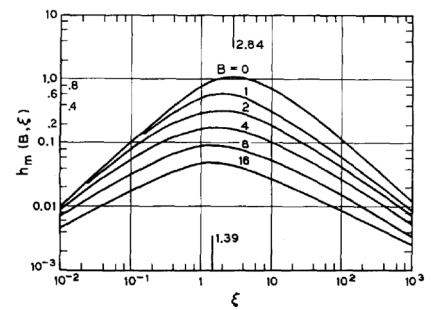


Figure 1.6: Résultats de Boyd & Kleinman pour le facteur de focalisation optimal

Instead of using:

$$h(\sigma, B, \xi) = \frac{1}{4\xi} \iint_{-\xi}^{\xi} \frac{e^{i\sigma(\tau-\tau')} e^{-B^2(\tau-\tau')^2/\xi}}{(1+i\tau)(1-i\tau')} d\tau d\tau'$$

and

$$h_m(B, \xi) = \max[h(\sigma, B, \xi)]_{\sigma}$$

They used

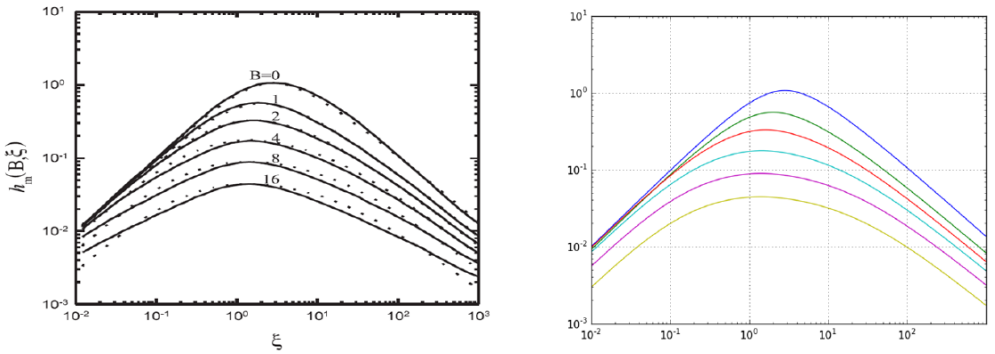
$$h_m(B, \xi) = \frac{h_{mm}(B)\gamma(B)\xi}{|\xi - \xi_m(B)|^{n(B)} + \gamma(B)\xi}$$

and

$$\gamma(B) = \frac{|\xi_m(0)|^{n(0)}}{h_{mm}(0)} e^{-B} + 13(1 - e^{-B/3})$$

with

$$\xi_m(B) = \frac{2.84 + 1.39B^2}{1 + 0.1B + B^2} \quad h_{mm}(B) = \frac{1.068}{1 - 0.7\sqrt{B} + 1.62B} \quad n(B) = \frac{1.91 + 1.83B}{1 + B}$$



(a) Résultat de l'approximation de Y.F. & Y.C. Chen (pointillés) et comparaison avec Boyd & Kleinman (ligne)

(b) Implémentation de l'approximation avec Python

Figure 1.7: Comparaison entre les résultats de Y.F. & Y.C. Chen et notre implémentation pour le facteur en SHG

This method is fast and gives good results for small walk off parameter  $B$  which is often the situation that one would seek in practical application. It can also be easily adapted to 2D for elliptical beam.

As we wanted to study the error on Chen's approximation, we tried to resolve the exact calculation with Python and what we found surprised us. After the maximum we were rapidly under what is predicted by Boyd & Kleinman, with already a difference of 60% at  $\xi = 10$  for  $B = 0$ . That is the reason why we studied the equation more in depth with the help of Mathematica. The equation 1.26 is far from being this straightforward, in fact when we ask Mathematica to integrate it, it gives us the following:

$$\begin{aligned} h_m(B, \xi) = & \frac{1}{4\xi} e^{-2\sigma_m} (-Chi((-1 - i\xi)\sigma_m) + Ci((1 + \xi)\sigma_m) - \log(i - \xi) \\ & + \log(-1 - i\xi) + Shi(\sigma_m - i\xi\sigma_m) - Shi(\sigma_m + i\xi\sigma_m)) \\ & (Ci((-i + \xi)\sigma_m) + i(\pi + iCi((i + \xi)\sigma_m) + Si((i + \xi)\sigma_m) - Si(i\sigma_m - \xi\sigma_m))) \end{aligned} \quad (1.27)$$

$Ci$  and  $Si$  are respectively cosine and sine integral functions and  $Chi$  and  $Shi$  are the hyperbolic form of those functions. This formulation can be resolved using the build-in piecewise adaptive Monte-Carlo algorithm and the results are in agreement with the calculations that we conducted previously in Python using the sinh-tanh quadrature as integration method.

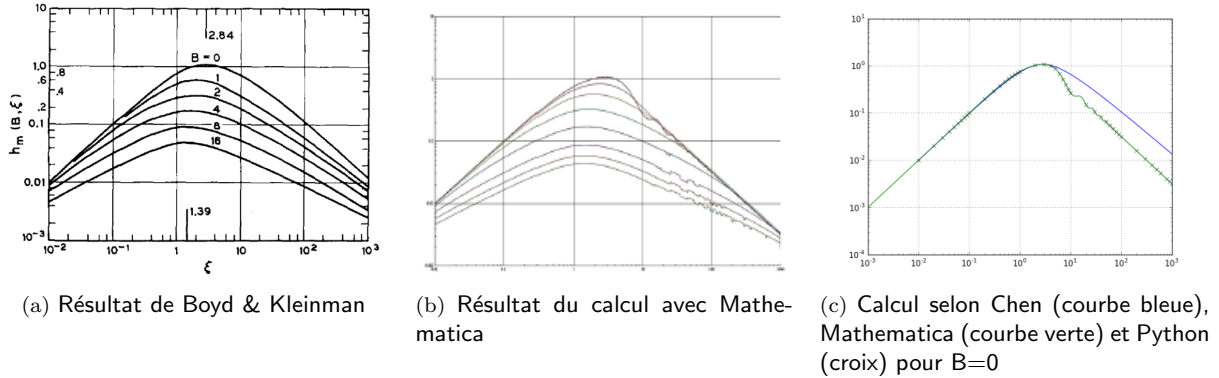


Figure 1.8: Comparaison des différents résultats du calcul du facteur de focalisation

From the above Figure we can see that the exact computation using Mathematica differs for small  $B$  and large  $\xi$ , and particularly for  $B = 0$ . This is because the equation being tedious to solve they assumed asymptotic behaviors with the following limits for thin crystals (no diffraction, no double refraction) and thick crystals (no diffraction):

	Thin crystal	Thick crystal
$\xi \ll 1$	$h_m(B, \xi) \rightarrow \xi$ for $\xi < 0.4$ and $\xi < 1/8B^2$	$h_m(B, \xi) \rightarrow \frac{\pi^{1/2}}{2} \xi^{1/2} B^{-1}$ for $\xi < 0.4$ and $\xi > 6B^2$
$\xi \gg 1$	$h_m(B, \xi) \rightarrow \frac{\pi^{3/2}}{4B\xi^{1/2}}$ for $\xi > 10$ and $4B^2 > \xi > \pi^2/16B^2$	$h_m(B, \xi) \rightarrow \frac{\pi^2}{\xi}$ for $\xi > 10$ and $\xi > \pi^2/16B^2$
$B \ll 1$	$h_m(B, \xi) \rightarrow 1.187\pi^2/\xi$ for $(80 < \xi < \pi^2/16B^2)$ when $B < 1/12$	

Table 1.1: Approximations faites par Boyd et Kleinman pour le calcul du facteur de focalisation

Y.F. & Y.C. Chen also presented analytical functions for Parametric Generation (PG) which is the other process described by Boyd & Kleinman in their paper. The same type of problem arises as the factor for PG (equation 1.28) is almost the same as for SHG.

$$\bar{h}(\sigma, B, \xi) = \frac{1}{4\xi} \iint_{-\xi}^{\xi} \frac{e^{i\sigma(\tau-\tau')} e^{-B^2\tau^2/\xi}}{(1+i\tau)(1-i\tau')} d\tau d\tau' \quad (1.28)$$

## 1.4 Quantum dots

A quantum dot is formed by embedding a lower band-gap semiconductor (blue in Figure 1.9) in a wider band gap semiconductor material (red in Figure 1.9), in this study these are InAs and GaAs respectively. To create a quantum dot the lower band-gap material has to be confined in all three dimensions, creating a so-called zero dimensional structure. The band gap is the energetic difference between the highest conduction band and the lowest valence band. If the volume of the structure is small enough, the energy of the charge carriers gets quantized as electrons and holes from the conduction and valence band are forced to be on discrete energy levels [27] (Figure 1.9.d), generally the smaller the dot the wider the band gap, that is why one can tune the emission of a particular dot by changing its size. Quantum dots are some nanometers big, but due to their discrete energy states they have similar properties as atoms, with the advantage that they are a solid state system.

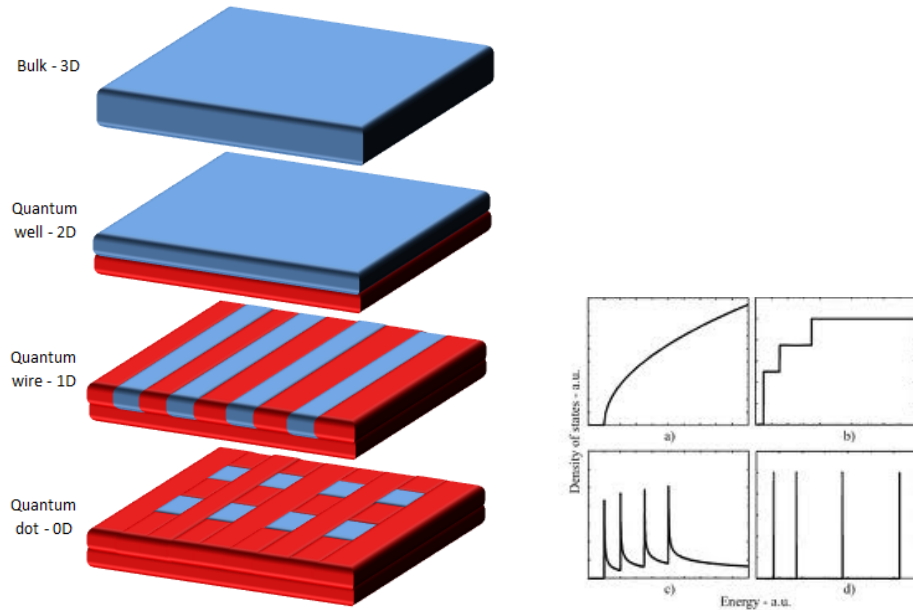


Figure 1.9: Confinement spatial et énergétique des nanostructures (de a.-bulk à d.-quantum dots)

Like atoms they can absorb and emit photons by respectively exciting and relaxing an electron upon an higher state. When the electron is excited he leaves a hole then the electron-hole pair recombines radiatively by emitting a photon. The decay rate depends on the wavefunction-overlap between electrons and holes. If there is one electron and one hole in the lowest band gap states, the quantum dot state it is called exciton ( $X$ ). The exciton energy is determined by the band gap of the material, the energies of the electron and hole ground states discussed above, and an additional term called the "binding energy" related to the Coulomb interaction (i.e. electrostatic interaction between two charged particles) between the electron and hole. When there are two electrons and two holes in the lowest possible band gap states, the quantum dot state is called biexciton ( $XX$  or  $2X$ ). A few possible configurations of electrons and holes in the lowest quantum dot states are shown in Figure 1.10.

The presence of another charge carrier in addition to the single exciton shifts the energy of the bound state due to Coulomb interaction. When adding charges of the same sign the energy shift can be estimated by first-order perturbation theory [28] [29]. Unfortunately, this method cannot be used for calculating the energy shift if a whole exciton is added to the system, but there are some numerical calculations which can describe the problem [30]. If one charge is added to an exciton, which means we have two electrons and one hole or two holes and one electron, we speak of a charged exciton or trion ( $X^-$  if there is an additional electron or  $X^+$  if there is an additional hole) as shown in Figure 1.10. The energy shift of the trion compared to the neutral exciton can be positive or negative. The biexciton energy  $E(XX)$  is usually lower than twice the exciton energy. This means, that the energy of the photon from the recombination of the first electron-hole pair is smaller than the energy of the second one, but also the opposite has been reported [31].

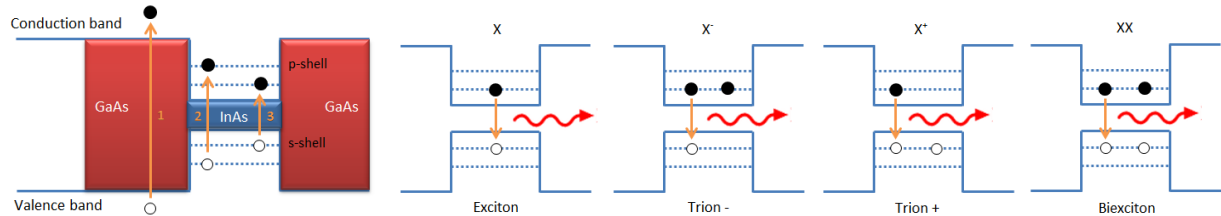


Figure 1.10: Excitation et relaxation d'une boîte quantique

If a state of a single quantum dot is populated, it has to decay and the state has to be repopulated before the same quantum dot can send out another photon. For this reason a quantum dot is a single photon emitter. If a higher state, for example a biexciton, is filled, the two states (e.g. biexciton and exciton) decay in a cascade, because the biexciton decays before the exciton. Which one of the two electron-hole pairs decays first is not significant, because they are indistinguishable. Exciton and biexciton have different recombination energies due to the Coulomb interaction.

The quantum dot can be excited optically in two ways. Either non-resonantly above the GaAs band gap with a laser whose energy is higher than the energy of the GaAs band gap, or resonantly with the quantum dot transition (as it is often done with atoms). In non-resonant excitation the laser is tuned above the band gap to create electrons and holes in the GaAs material surrounding the quantum dot. Some of these carriers get captured by the quantum dot and relax to the quantum dot ground state via phonon emission [36]. This is a very convenient excitation scheme, because enough charge carriers can be created in the surrounding material to fill almost all the possible quantum dot states. With this kind of excitation it is rather easy to filter out any reflected excitation laser from the quantum dot emission for example by placing a long pass filter in the optical path after exciting the quantum dot. This is a requirement if we use collinear, confocal excitation and collection in our setup that has a resonant excitation scheme. The different types of excitation are presented in Figure 1.10.

## 2 Experimental set-up

The entire experimental set-up consists of three main parts which perform three different processes. The first one is the source for generating single-photons, in this study we will address the details of the SPDC source and introduce the quantum dots (QD) source. The second process is the three-path interferometer where all the configurations corresponding to each constituents of the interference terms are performed for us to evaluate them. The third one consists of the acquisition and use of the data. All experimental set-ups and hardware that were build during this thesis will be discussed but a special emphasis will be given to those related to the heralded single-photons source.

The SPDC system is constituted of the following parts:

- An heralded single-photons source for generating a beam out of a  $\chi^{(2)}$  non-linear crystal of PPKTP
- An oven to control crystal temperature to maximize SPDC efficiency
- A counter to detect the photons counts, singles and coincidences

The QD source is composed of a laser exciting the QD embedded in a cryostat from the side. The emission from the QD is then collected from the top and sent to the three-paths set-up.

The interferometer part is composed of:

- A three-paths set-up to perform Born's rule test
- A slits system with its controller

After doing some studies on the subject and its theory, we started to build an oven for the PPKTP crystal in order to perform temperature tuning and enhance the conversion efficiency. Once that done, we build the heralded single-photon source and a counter to measure coincidences. While doing all of that, we also started the fabrication of new shatter systems which have now five slits. We build the controller for these shatters and wrote a script to assure their proper working order. Then after setting up the whole system we tested it with an 808 laser and the old shatter system. Finally we tested it with single-photons sources.

### 2.1 SPDC system

As science aims toward quantum communication technologies the need for manipulating and counting photons individually became crucial. Before quantum optics, emission and detection of single photons was obtained by attenuating a laser beam until so few photons were emitted that one was able to count them. But this is more a "no-photons" source with occasional single-photons detection than a single- one because the vacuum probability (no detection) is higher than the probability to detect a photon. Also the probability to detect two photons, although very small, was not zero [32].

Single-photons sources are nowadays constructed by many means: photonic materials, non-linear optics, single isolated emitter, nano-semiconductor devices, impurities in diamond,... [33] Those means can be regrouped in two types, one way is to obtain a single photon through excitation and relaxation of an isolated system such a quantum dot by example, the other way is to produce a bi-photon field, known as heralded or correlated photons where the detection of one photon indicates the existence of the second.

### 2.1.1 Temperature controller

The PPKTP crystal has an energy threshold which is the limit where the intensity of the input beam reaches the point where it generates gray tracks, a type of color centers. Color centers are crystallographic defects generated by high temperature which causes electrons to get displaced. When they fill an anionic vacancy in the crystal they tend to absorb light in the visible spectrum so that the crystal which is usually transparent becomes colored. This problem can be avoided by heating the crystal so that there is no accumulation of electrons in vacancies (the extra energy places them homogeneously). Heating up a PPKTP crystal also extends its lifetime and can increase the intensity of the generated beam, but the crystal has also a temperature threshold around 170°C above which it experiences photo-refractive damage when it absorbs so much energy that it melts and recrystallize. This is a critical damage that reduces the conversion efficiency and therefore the generated beam quality, in our case it cannot be reversed.

In order to tune the temperature we build an oven based on the HTC1500 temperature controller from Wavelength Electronics. The oven is composed of an aluminium structure on a Peltier element with a sensor connected to a driver circuit which controls the temperature in function of the voltage applied to the Peltier element.

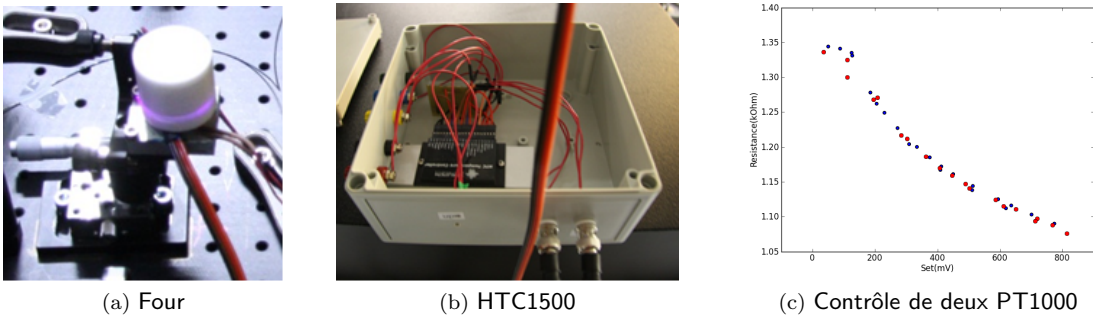


Figure 2.1: Photographies du four et du contrôleur de température et vérification du contrôle

Once we build the oven we first checked that it was responding well to the voltage control. According to the data sheet of PT100 and PT1000 the response of the temperature sensors should have a quadratic form, this is what we observe in Figure 2.1c. Once the crystal is introduced into the oven one has to determine the optimal temperature to produce the desired beam at the highest efficiency. There are two main methods to find it, performing temperature tuning or back align with an 808 nm laser and optimize the 404 nm output beam intensity resulting from the SHG. Those two measures are discussed later on in 2.1.4. Finally we placed the PPKTP crystal into the oven and heated it up to 33°C corresponding to 112.8 Ohm for a PT100 with a temperature stability of 0.01°C.

### 2.1.2 Heralded single-photons source

The principle of SPDC was already described in 1.2.1 and the effect is quite easy to obtain. But there are still two main problems remaining to perform a perfect theoretical test. The first problem is that it is not an "on-demand" source as it produces a random number of single-photons. The second problem is again that the single character is not guaranteed, especially at high gain regimes [34]. Besides, lack of high brightness of the source, and imperfect detector characteristics such as detection efficiency, dark count rate, timing jitter and dead-time, significantly limit the photons detection rate. That is why a special attention must be accorded to the minimization of all those limitations during the realization of an HSPS. Here we present the realization of an HSPS based on the SPDC of a 404 nm incident beam into a 808 nm resultant beam in a PPKTP crystal.

## PPKTP

Potassium titanyl phosphate ( $\text{KTiOPO}_4$  - KTP) was first synthesized in 1890 by L. Ouvard [35] but it is only in 1976 that Zumsteg, Bierlein and Gier identified the non-linear optical properties of this crystal [36]. KTP presents good properties such as high non-linear coefficients, high damage threshold and non-hygroscopicity (i.e. it does not attract water) which allow us to use it for optical applications requiring high power, high efficiency and durability.

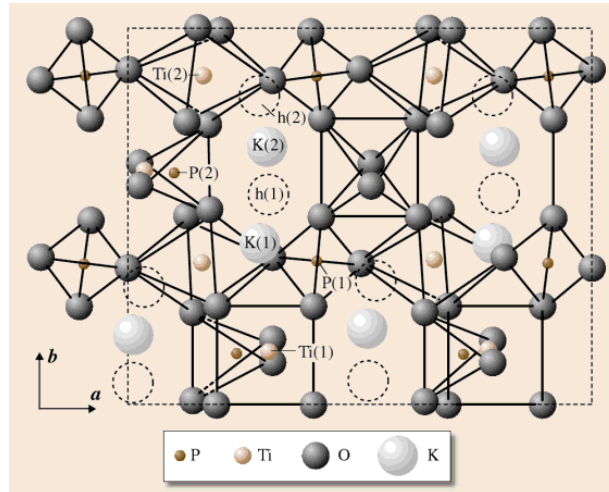


Figure 2.2: Structure d'un cristal de KTP tiré de [37]

KTP has an orthorhombic structure characterized by octahedral chains of  $\text{TiO}_6$  linked at two corners by alternating long and short Ti-O bonds that give rise to the large non-linear optical effects observed in KTP because of the asymmetry that gives a preferential direction of polarisability. The constant growth rate of the hydrothermal process insures homogeneity throughout the crystal bulk. KTP is optically transparent from 350 nm to 3.5  $\mu\text{m}$ . The optical spectrum is structure-free except for traces of OH-absorption bands observed at 2.8  $\mu\text{m}$  and 3.8  $\mu\text{m}$ . Crystals with little or no scatter have been produced with very low strain. Damage thresholds have been measured well in excess of 1  $\text{GW}/\text{cm}^2$ . The refractive indices vary slowly with changes in wavelength and temperature. The non-linear optical coefficients are comparable to those of  $\text{Ba}_2\text{NaNb}_5\text{O}_{15}$  and KTP can be phase matched at 1.06  $\mu\text{m}$  using either Type I or Type II interactions. In Type II interactions that we use, KTP has large angular and temperature bandwidths as well as high non-linear coefficients and damage thresholds. It has a high conversion efficiency for SHG of laser light with fundamental wavelengths between 994 nm and 2.5  $\mu\text{m}$ . This material is also well suited for use as an optical parametric oscillator (OPO). KTP wide tuning range and high conversion efficiency mean that short crystals can be used in this application. Another application well suited for KTP is quasi-phase matching (QPM) as described in 1.2.2.

An indication of the non-linearity of a  $\chi^{(2)}$  crystal will come from the polarization matrix (eq. 2.1) which describes the interaction between a beam and such a crystal. The components of the  $d$  matrix are non-linear coefficient tensors of the material and can be directly related to the susceptibility tensor (equation 2.2).

$$\begin{bmatrix} P_x(2\omega) \\ P_y(2\omega) \\ P_z(2\omega) \end{bmatrix} = 2\epsilon_0 \begin{bmatrix} d_{11} & d_{12} & d_{13} & d_{14} & d_{15} & d_{16} \\ d_{21} & d_{22} & d_{23} & d_{24} & d_{25} & d_{26} \\ d_{31} & d_{32} & d_{33} & d_{34} & d_{35} & d_{36} \end{bmatrix} \begin{bmatrix} E_x^2(\omega) \\ E_y^2(\omega) \\ E_z^2(\omega) \\ 2E_y(\omega)E_z(\omega) \\ 2E_x(\omega)E_z(\omega) \\ 2E_x(\omega)E_y(\omega) \end{bmatrix} \quad (2.1)$$

$$d_{ijk} = \frac{1}{2}\chi_{ijk}^{(2)} \quad (2.2)$$

The non-linear coefficients for a particular crystal such as KTP can be found in table such as in [21].

To achieve QPM with KTP the most widely used method is periodic poling. Periodic poling of non-linear crystals is a technique used to obtain a reversal of magnetic domain orientation so that the non-linear coefficient also reverses. This makes a quasi-phase matching as seen in 1.2.2 which increases the efficiency of the heralded photons production.

KTP crystal can be grown using two techniques, hydrothermal and flux growth. The hydrothermal process crystallizes substances from high-temperature aqueous solutions under high pressures in autoclave. It produces large, good-quality crystals with good control over the composition but autoclaves are expensive and it is impossible to monitor the crystal while it grows. The flux method crystallizes components dissolved in a solvent (the flux) by cooling them to room temperature. There is no polishing of the created crystals needed because they grow with natural facets making them interesting for optical applications but this method produces relatively small crystals. Once the crystal is grown it has to be periodically poled in order to achieve QPM. Here we will address some important methods to achieve periodic poling

Gupta et al. (1993) demonstrated that an electron beam could be used for periodic poling of KTP [38]. They made a 0.5 mm long fifth-order domain-inverted grating (20  $\mu\text{m}$  period) in a 1 mm thick hydrothermally-grown KTP crystal using an electron beam and demonstrated frequency-doubling of Ti:S laser tuned to 840 nm. Chen and Risk (1994) reported periodic poling of hydrothermally-grown KTP crystal using an electric field applied to a periodic (4  $\mu\text{m}$  period) metal electrode [39]. They observed that the electric-field strength required to produce domain inversion in KTP was only about 2 kV/mm, an order of magnitude lower than the value required for lithium niobate (LN). This relatively low electric field permitted poling of thick ( $\sim 1$  mm) crystals in the ambient atmosphere without causing breakdown of the surrounding air, making it convenient to monitor the poling process using SHG or interferometry.

Flux-grown KTP is less expensive than hydrothermally-grown KTP and is available in larger sizes. But it has a higher ionic conductivity, which makes electric-field poling more difficult. Rosenman et al. (1997) studied the domain inversion process in flux-grown KTP and found conditions under which an applied electric field could produce domain inversion [40]. Oron et al. (1997) applied this process to make first-order gratings (6.9  $\mu\text{m}$  period) for SHG of 980 nm lasers in 0.5 mm thick flux-grown KTP crystals and achieved a bulk SHG efficiency of 4.6 %/W/cm. Flux-grown KTP periodically poled by this technique has been used for high-efficiency single-pass SHG of a pulsed, diode-pumped Nd:YAG laser (Englander et al., 1997) and for resonant doubling of a continuous wave Nd:YAG laser (Arie et al., 1998). Another approach to periodic poling of flux-grown KTP has been reported in which ion-exchange is first used to reduce the conductivity at the surface of a KTP crystal, then an electric field is applied to a periodic electrode in order to create a domain-inverted grating (Karlsson and Laurell, 1997) [41]. A grating with a period of 9  $\mu\text{m}$  has been used to demonstrate first-order SHG with a 1064 nm Nd:YAG laser, and this approach generated 2.9 mW of 532 nm light from 890 mW of pump power. Periodic poling has also been induced by stress using a dielectric cladding (Buritskii et al., 1993) [42].

As we seen there are many ways to periodically pole a non-linear crystal but the most common technique to achieve periodic poling of non-linear crystals is by ferroelectric domain engineering. Typically, a pattern of electrodes induces strong electric field into the material (ferroelectric crystals) to create the desired ferroelectric domains. Usual materials to be poled are lithium niobate (LN,  $\text{LiNbO}_3$ ), lithium tantalate (LT,  $\text{LiTaO}_3$ ), potassium titanyl arsenate (KTA,  $\text{KTiOAsO}_4$ ) and of course potassium titanyl phosphate (KTP,  $\text{KTiOPO}_4$ ). The electrodes are usually made during a photo-lithographic process. The poling period which in this case is the period of the electrode pattern determines the wavelengths for which certain non-linear processes can be quasi-phase-matched, and therefore the conversion efficiency increased.

One of the main advantage of periodic poling is that one can relatively choose the period of the electrodes pattern so that the periodic modulation allows QPM for a wide range of wavelengths in the domain of transparency of the crystal. Another advantage is that the direction of propagation and the polarization of the beams can be chosen so that  $d_{eff}$  is maximized and the walk-off minimized in order to maximize the interaction length.

The main limitations of the method are that the field to be applied must be larger than the coercive field strength which is typically in the order of 1 kV/mm or higher. This limits the thickness of samples. Thick ones ( $> 0.5$  mm) will be only poled near the electrodes. Another limitation which also concerns the size is that it is difficult to manufacture and connect electrodes smaller than 10  $\mu\text{m}$ . This is why it is challenging to achieve high poling quality for small poling periods or thick samples.

The crystal that we used is of dimension 2x1x10 mm, it is made using the flux grown technique. Here we will summarize the crystal properties for the parameters used in the experiment described in this work. With a pump wavelength of  $\lambda_{2\omega} = 404$  nm, a generated wavelength of  $\lambda_\omega = 808$  nm, a period length of  $\Lambda = 9.825$   $\mu\text{m}$ , a crystal length of  $L_c = 10$  mm and a thermal expansion coefficient of  $\alpha = 0.6 \cdot 10^{-6}$ , the temperature bandwidth is  $\Delta T = 1.05^\circ\text{C}$  and the angular bandwidth of  $\Delta\theta = 0.059$  rad =  $3.38^\circ$ , assuming normal incidence. Thus, a temperature change of  $0.5025^\circ\text{C}$  or a change of the incident angle of  $1.69^\circ$  can halve the power of the beam generated.

### Gaussian Beam Propagation and ABCD method

Once everything ready with the crystal and the oven we began to build the source. To do so we used the ABCD matrix formulation to find the emplacement and size of the waist of the beams in order to place the crystal and to couple with two collimators to collect the heralded generated photons.

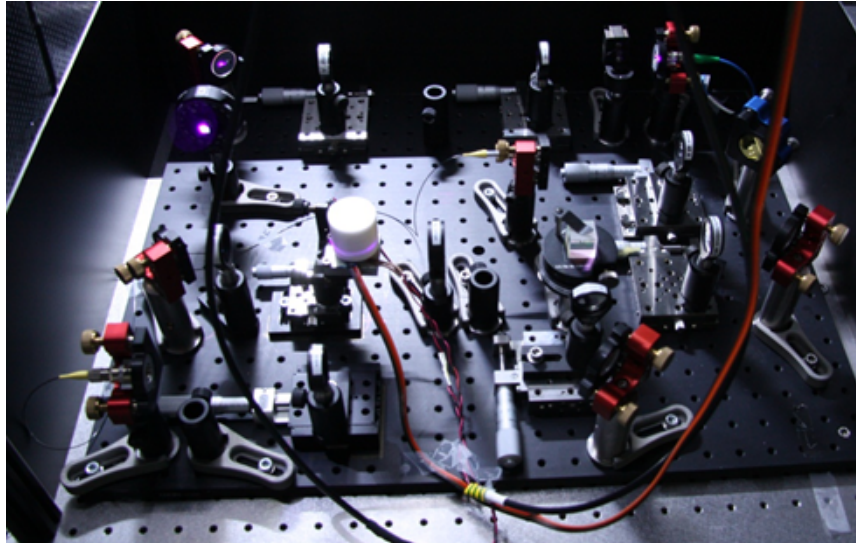


Figure 2.3: Photographie de la source de photons corrélés

The z-propagating Gaussian beam with a wave-number  $k = \frac{2\pi}{\lambda}$  satisfies the Helmholtz wave equation 2.3 which has equation 2.4 for solution.

$$(\nabla^2 + k^2)u = 0 \quad (2.3)$$

$$u(r) = \psi(r)e^{ikz} \quad (2.4)$$

Under the paraxial approximation the spatial propagation term  $\psi(r)$  admits the following solutions:

$$\psi \propto \exp \left[ i(p(z) + \frac{k}{2q(z)}(x^2 + y^2)) \right] \quad (2.5)$$

Here  $p$  is the complex phase shift in function of the beam propagation.  $q$  is the complex beam parameter describing the beam in a position  $z$  as defined in eq. 2.6. The  $q$  parameter is very important in the description of ray optics with Gaussian beams. It is composed of two parameters,  $R$  is the radius of curvature of the phase front and  $\omega$  is the beam width at a certain position. This beam width can be found at any point once we know the beam waist size  $\omega_0$  (eq. 2.7).

$$\frac{1}{q} = \frac{1}{R(z)} - i \frac{\lambda}{\pi \omega(z)^2} \quad (2.6)$$

$$\omega(z) = \omega_0 \sqrt{1 + \left( \frac{z\lambda}{\pi\omega_0} \right)^2} \quad (2.7)$$

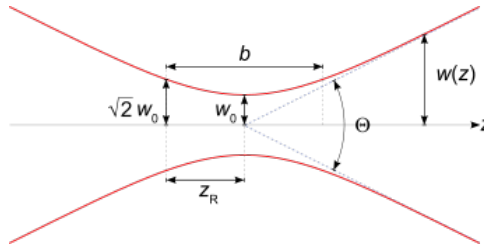


Figure 2.4: Schéma du waist et paramètres importants

The divergence of the beam can be characterized by the confocal parameter  $b$  which is the length where the beam size changes from  $\sqrt{2}\omega_0$  to  $\omega_0$  and back to  $\sqrt{2}\omega_0$  again.

$$b = 2z_R = \frac{2\pi\omega_0^2}{\lambda} \quad (2.8)$$

Since the output power increases with input intensity, if the input power is kept steady one can think that strong focusing into the crystal will only improve the effect. But tight focusing can provoke severe damage to the crystal and reduces the interaction length. According to Boyd and Kleinman as extensively seen in 1.3 there is an optimum focusing in order to increase the conversion efficiency.

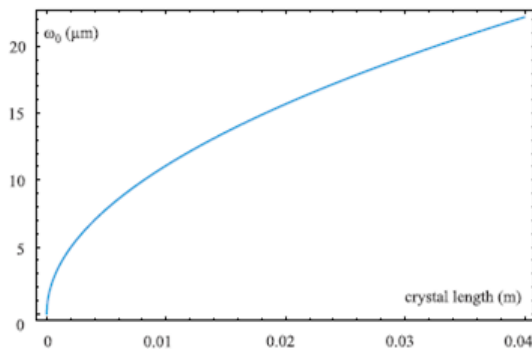


Figure 2.5: Taille du waist optimale pour une efficacité de conversion maximum d'un faisceau à 404 nm

The optimum size of the waist inside the crystal that as a length of 0.01 m is about  $2 \times 12 = 24 \mu\text{m}$ , we choose a looser focusing of about  $30 \mu\text{m}$ . As we wanted a waist of about  $30 \mu\text{m}$  inside the crystal we will have an output beam size of about  $\sqrt{2} \times 30 \approx 42 \mu\text{m}$ .

We measured the  $q$  parameter of each of the collimators that we wanted to use and calculated the positions at which we had to put all of our components with the ABCD matrix system.

The ABCD matrix formulation allows to take into account all the components of an actual set-up into the beam description to be able to know the properties of the beam all along its propagation. This allows performing quick calculation on where to put several optical components to collimate the desired output beam. The beam propagates through an optical system following the ABCD ray transfer matrix (eq. 2.9) which is often expressed in its reciprocal form equation (eq. 2.10) for convenience.

$$q_2 = \frac{Aq_1 + B}{Cq_1 + D} \quad (2.9)$$

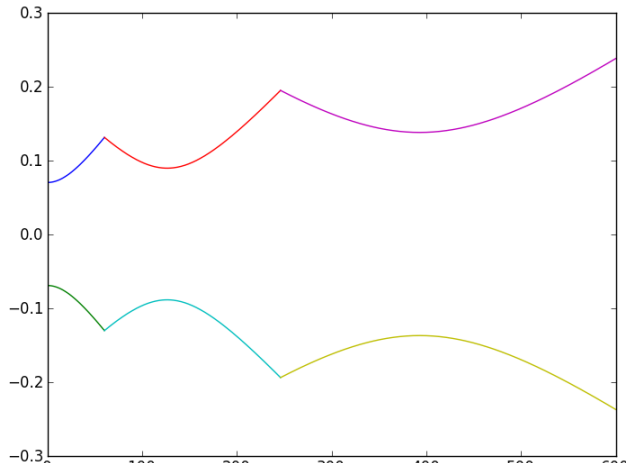
$$\frac{1}{q_2} = \frac{C + Dq_1}{A + Bq_1} \quad (2.10)$$

At each optical component can be attributed a correspondent transfer matrix. The few ones that we used are listed below:

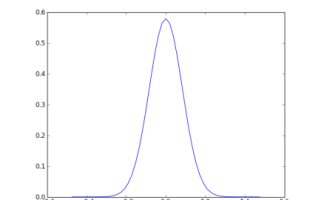
- Free space propagation  $\begin{pmatrix} 1 & d \\ 0 & 1 \end{pmatrix}$   $d$  distance
- Reflection at a flat interface  $\begin{pmatrix} 1 & 0 \\ 0 & \frac{n_1}{n_2} \end{pmatrix}$   $n_1$  and  $n_2$  initial and final refractive indices
- Reflection at a flat mirror  $\begin{pmatrix} 1 & 0 \\ 0 & 1 \end{pmatrix}$
- Thin lens  $\begin{pmatrix} 1 & 0 \\ -\frac{1}{f} & 1 \end{pmatrix}$   $f$  focal length

As multiplication of matrices is non-commutative, matrices of different components must be ordered properly with the last matrix pre-multiplying the second last and so on until the first one.

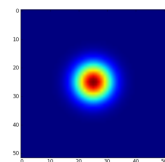
Example of a two lenses system:  $q_z = \begin{pmatrix} 1 & d_3 \\ 0 & 1 \end{pmatrix} \begin{pmatrix} 1 & 0 \\ -\frac{1}{f_2} & 1 \end{pmatrix} \begin{pmatrix} 1 & d_2 \\ 0 & 1 \end{pmatrix} \begin{pmatrix} 1 & 0 \\ -\frac{1}{f_1} & 1 \end{pmatrix} \begin{pmatrix} 1 & d_1 \\ 0 & 1 \end{pmatrix}$



(a) Propagation du faisceau gaussien en mm



(b) Profil du faisceau à  $z = 600$  mm



(c) Spot à  $z = 600$  mm (intensité normalisée)

Figure 2.6: Example de résultats d'un calcul ABCD pour un système à deux lentilles

In Figure 2.6 we see an example of the propagation of a Gaussian beam with  $\lambda = 404$  nm in a two lenses system, the source being a collimator with  $1/q = -0.026419720553i$ . The lenses are at positions 60 mm for the first one which has a focal length  $f = 50$  mm and 246 mm for the second one of  $f = 100$  mm. On the right side one can see the characteristics of the spot in normalized intensity at detector position  $z = 600$  mm. The python code can be found in Appendix B.1.

So we measured the  $q$  parameter of our three collimators with the beam profiling method for three two-lenses systems and we found with the ABCD program where the lenses had to be placed in order for the waists of all arms to be overlapping at the center of the crystal. We approximated the other optical components as being an extra length of the path due to a refractive index superior of 1.

Once we had the proper position we placed all the components first by aligning the input beam for the waist to be in the center of the crystal. Once it produced SPDC we back aligned with an 808 nm laser to overlap the 404 nm input beam. In order to further improve the coupling we finished by doing some beam walking. Finally it looks like Figure 2.7.

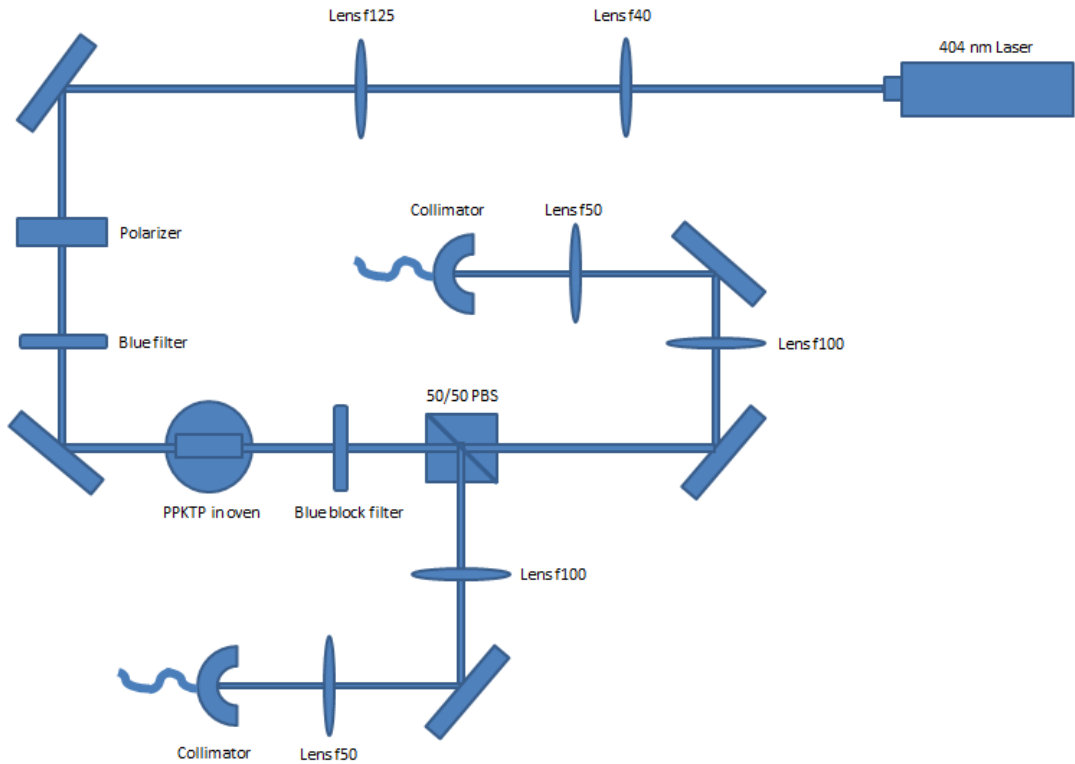


Figure 2.7: Schéma de la source de photons corrélés

To comment Figure 2.7 and summarize the overall source set-up, first the input beam comes from a 404 nm blue laser diode and then it is collimated through two lenses. A polarizer assures that only horizontally polarized photons are passing through as they are the only one able to induce the SPDC effect in PPKTP. The first version of the source had a polarized beam splitter instead of the polarizer and we did our first measurement with it but there were some transparency problems as it was not made for 404 nm but for 450 nm. We then rebuild the entire source with the polarizer because it made a different optical path. It is followed by a blue filter which lets only pass 404 nm in order to narrow the wavelength dispersion of the beam. The crystal is placed in the waist, with the waist in its center to maximize SPDC efficiency. Then a blue block filter cut the pump component of the beam resulting from the interaction with the PPKTP to let only pass the generated beam at 808 nm.

This beam goes then into a 50/50 polarized beam splitter (PBS) where the two heralded photons are split as one is horizontally polarized and will be transmitted while the other vertically polarized will be reflected (as explained in 1.2.2 it is a type II effect). Each of the two beams are then collimated again by two lenses and finally collected through collimators into avalanche photo-diodes (APDs) that count incoming photons by converting them into electrical pulses.

### 2.1.3 Coincidences counter

Once the 808 nm photons being detected by the APDs we build a counter in order to find the coincidences. The APDs provide electrical counts to the detection circuit. The signal and idler counts are read by Perkin-Elmer detectors which have an output of about 25 ns long and a 2.5 V high voltage pulse output. To measure the coincidences we used a AND gate. An AND gate is a basic logic gate that compares two binary values and delivers as output the minimum between them. That means that the AND gate will only give a high output when both of the inputs are also in high voltage state or in binary notation the value 1. Two 1 in both inputs means that both inputs have detected a photon, there is a coincidence.

The only problem of this configuration is that the pulses coming from the detectors are too short for the circuit. One needs to increase the duration of the pulse without introducing losses. This process is called pulse stretching and is easy to achieve using flip-flops. A flip-flop also called a latch is a circuit that has two stable states that can be changed by applying a signal in one or more inputs and will be recovered in one or two outputs. This is used to store the state information making this circuit a fundamental building block of modern electronics. Here D flip-flops have been used, D stands for data or delay, they can be viewed as memory cells, zero-order holds or delay lines. The D flip-flop takes the signal on the D input pin while the flip-flop is clocked so that changes on the D input will be ignored until the next clock event. The AND function can also be implemented using flip-flops.

The schema of the circuit can be found in appendix. We used five D flip-flops in the circuit, they correspond to five of the six sides of three TTL (Transistor-Transistor Logic) chips, black blocks on Figure 2.8. TTL chips are a class of digital circuits built upon bipolar transistors and resistors. They tend to disappear because while fast they also have an high energetic consumption and now CMOS circuits can be more efficient and tend to replace them in today's electronic. Here we will call those TTL sides D1, D2, ..., D5 for better comprehension.

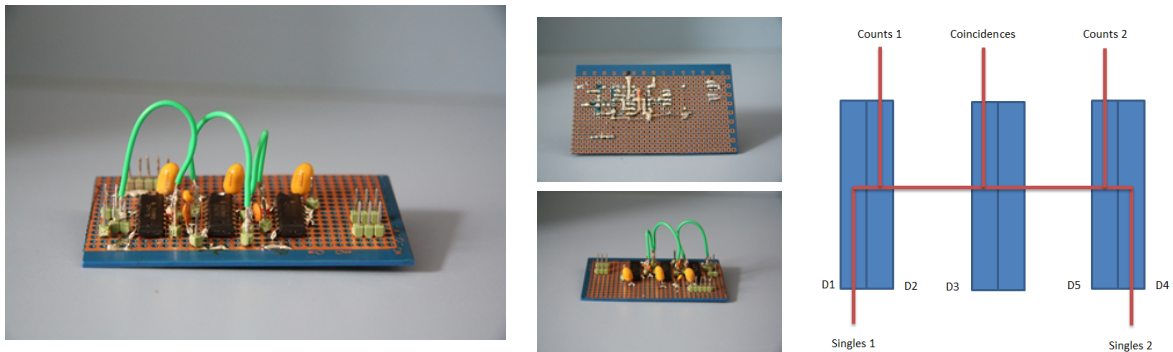


Figure 2.8: Photographies et schéma du circuit compteur de coincidences

The two detector outputs arrive onto the stages in D1 and D4 where they are first reduced in length to about 10 ns. Beyond reducing the pulse duration D1 and D4 also serve to increase the pulse height. Outputs of these two flip-flops go into D2 and D5 for pulse shaping in order to read the single counts from their outputs. They also go into D3 to perform the coincidence detection. One can follow the action of the circuit on the schematics in Appendix C.1 or on the schematics from Figure 2.8.

Note that the coincidence counter is implemented as a D flip-flop so that the data line has to be high at the arrival of the clock signal in order to measure coincidence. That means that the clock signal has to be delayed with respect to the data signal or in other words, since the circuit is symmetric, the detector's signal has to come sometime earlier on D1 than on D4 or vice-versa. Measurement of the circuit output shows that an output pulse is produced on D3 if this delay is between 1 and 9 ns. We see that ideally the signal of the first detector should be about 5 ns ahead of the other channel because the coincidence window is about 8 ns long. If one would reduce the coincidence window he will just have to apply a voltage divider on the outputs of D1 and D4 and then feed the divided voltage into D3. The inputs of D2 and D5 can still be derived from the full outputs of D1 and D4 since these are for pulse stretching only. The required 5 ns delay can easily be gotten by using an extra 1 m of BNC cable in the connection between the detector and the circuit. The outputs of D2, D3 and D5 are about 150 ns long high TTL pulses. If necessary, the duration of these pulses can be changed by choosing a different value for the resistors R1, R2, R3, or the capacitors C1, C2, C3 (Appendix C.1).

One of the main limitations of such a circuit is that the TTL circuits must be alimented at  $5V \pm 5\%$ , any short circuit or bad power alimentation will seriously deteriorate the counter.

In the schematics from the appendix, a couple of by-pass capacitors are not shown. They should, however, still be in the circuit in order to avoid high-frequency transients. A transient is the voltage that appears after current interruption. It can give a false reading of the pulses length this is why they have to be as limited as possible. The value of these capacitors is  $10 \mu F$ . Since these capacitors connect the power to the ground, they can be polarized. The power itself is derived from the counter board USB-4303 from Measurement Computing. This board also collects the three signals, single counts and coincidences counts to be monitored on the computer. The data sheet of the USB-4303 can be found at <http://www.mccdaq.com/PDFs/Manuals/USB-4303.pdf>



Figure 2.9: USB-4303

#### 2.1.4 Characterization of the source

Once the source build, we needed to characterize it in order to use it at its best. To do so one could firstly check the visibility (equation 2.11) to find the best angle of the polarizers to have the optimum polarization in order to increase the coincidence count rate. It should look like Figure 2.10 taken from [32] but in our case we preferred to measure the polarization of the beam in front of the crystal after the polariser in order to directly maximize the horizontal fraction that induces SPDC going through.

$$V = \frac{I_{max} - I_{min}}{I_{max} + I_{min}} \quad (2.11)$$

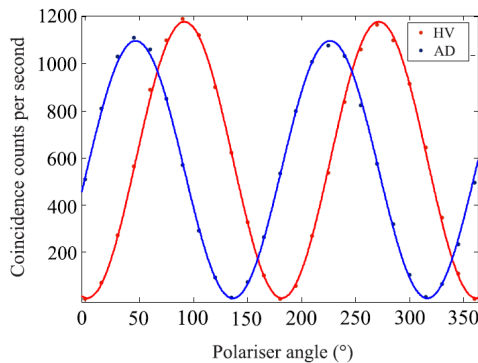


Figure 2.10: Mesure de la visibilité pour les polarisations HV (horizontal - vertical) et AD (anti-diagonal - diagonal)

Another test can also be to study the dependence of singles and coincidence count rate upon input power to see if one arm produces more pairs than the other. Results of this test are shown in Figure 2.11. It should have a linear evolution but the singles counts do not start from 0 because of the detectors dark counts. Also it was dangerous to use more than 10 mW as it could deteriorate the crystal. This measures gives the overall quality of the source and allow us to have a better insight on compensating the power fluctuations by giving us the efficiency in each arm of the source.

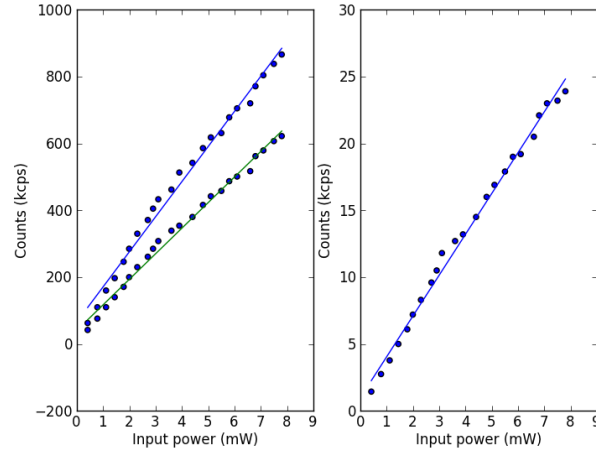


Figure 2.11: Dépendance de la génération de photons en fonction de la puissance du signal de pompe

The spectral distribution of the generated beam can also be recorded on a spectrometer to be able to perform some frequency tuning. As angle tuning is much more difficult to perform than temperature tuning, we studied changes in wavelength for different temperatures (Figure 2.12a). We also can extract an indication of the temperature tolerance from the Figure 2.12b which shows the phase matching function of the SHG generation of our source.

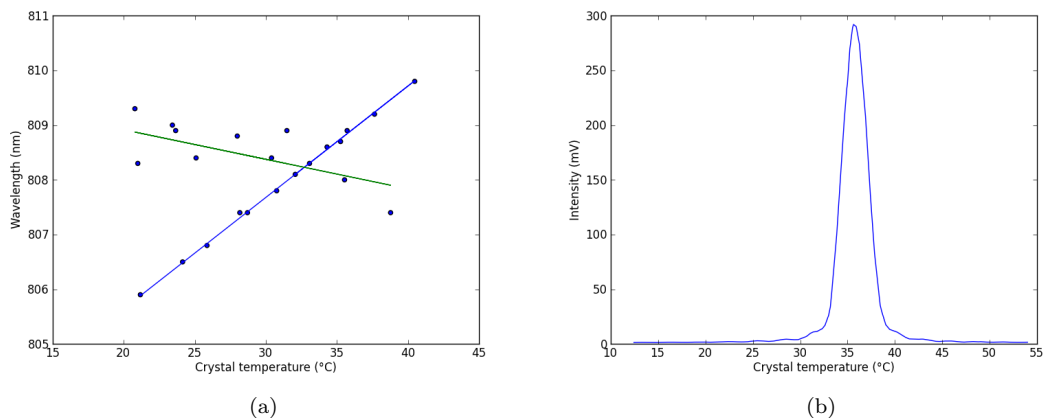


Figure 2.12: Effet du changement de température sur la longueur d'onde du faisceau généré

We can see from those two measures that the optimum temperature is different between SPDC and SHG. The phase matching function was simply acquired by sending a beam back at 808 nm from one of the arm used to collect and then we collect the intensity of the beam generated on an APD from the first collimator. Because the crystal is not perfectly symmetrical along its z axis, shooting the input beam from one end of the crystal or the other will have an effect upon the generated beam and upon the wavelength detuning. Moreover one can clearly see the form of the *sinc* function which shapes the power of the generated 404 nm beam.

Another study of interest would have been to look at its second order of coherence with a study of the function  $g^{(2)}$  [43] which is generally expressed as in equation 2.12 and gives an indication of the single-photon character of the source see [33] [34] for references.

$$g^{(2)}(\tau) = \frac{\langle I(t)I(t+\tau) \rangle}{\langle I(t) \rangle^2} \quad (2.12)$$

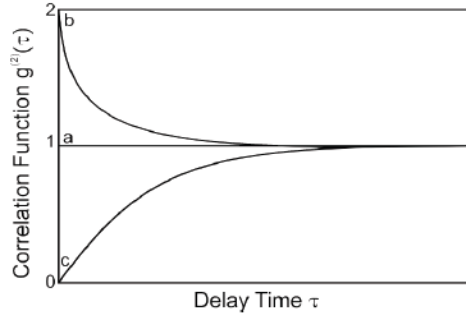


Figure 2.13: Allure générale de la fonction  $g^{(2)}$  pour une source laser (a) et une source de photons uniques (c) [44]

## 2.2 Quantum dot source

The easiest way one could think of fabricating a quantum dot is to grow a thin layer of one semiconductor material on the wider band-gap material and etch away material in lateral directions to reach confinement. This method is possible [45] but unfortunately the structures are usually not small enough to confine only one electron [46]. Typical growing techniques are cleaved-edge overgrowth, patterned growth, and self-assembled quantum dots. Our sample being self-assembled, I first give a short explanation of what self-assembled quantum dots are.

The dots are self-assembled quantum dots or so-called "Stranski-Krastanow" quantum dots [47]. They are bottom-up grown dots which are relatively easy to fabricate because their growth does not need any patterning or etching [46]. The method used for growing is molecular beam epitaxy (MBE) [48]. The MBE procedure works as follows: For each element of the desired compound there is a source in which the element is brought into the vapor phase and an effusive beam is created. These beams are set up so that they are directed towards a crystalline substrate. This way the different materials can be deposited on the substrate in a controlled way via shutters and temperature control enabling the growth of monolayers.

For the samples used in this thesis InAs (which is the material with the lower bandgap) was deposited on GaAs. Between InAs and GaAs there is a lattice mismatch of about 7% [49]. In the growth procedure, first a thin layer of InAs is deposited on GaAs, forming the so-called wetting layer. After a critical thickness of the layer is reached, the strain in the material becomes big enough that the material forms little islands spontaneously. These islands are typically 4-7 nm thick and 20-40 nm in diameter, depending on growth conditions [49]. To have the lower bandgap material surrounded in all directions, the islands are overgrown with another layer of GaAs (see Fig. 2.14). The positions of the dots are random, but still one can control the density and sizes of the quantum dots by choosing the amount of material deposited, the deposition rate, and the growth temperature.

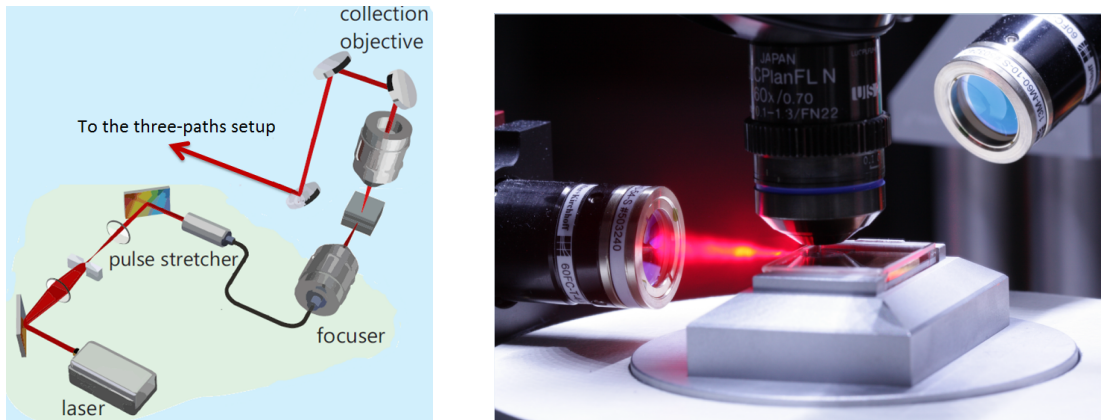


Figure 2.14: Schéma et photographie du processus d'excitation/collecte des boîtes quantiques

The sample are excited with light derived from a continuous wave (CW), mode-locked, and wavelength tunable Ti:Sapphire laser. When needed the same laser can be set to be pulsed. Figure 2.14 shows the schematics of the excitation and a picture of the setup.

One can use a first beamsplitter before the sample to reflect a part of the laser beam to a photodiode. This diode is used for recording the power of the excitation beam for power dependent measurements. Another beamsplitter is used when the sample is excited co-linearly (from the top). This scheme of excitation is called co-linear because the excitation beam and the collected photoluminescence take the same path. The quantum dot sample is placed inside a continuous-flow liquid-helium cryostat with separate optical windows for excitation (side) and collection (top) and its emission is collected with a x60 microscope objective from above (along the growth direction, orthogonal to the excitation plane). The emission is directed to the analysis part, where various measurements are done for different experiments.

If possible multimode fibers are used to bring the generated beam to the interferometer set-up because more emission is collected as they are easier to align. When the emission lines are too close to each other in the spectrum, singlemode fibers are the proper choice. With multimode fibers lines with a wavelength distance of more than 1 nm can be resolved. With singlemode fibers a ten times higher resolution can be achieved since they have a smaller fiber core.

The dots on the sample are called "bare" dots because they are not embedded into a cavity. The sample has a low dot density of about  $10 \text{ dots}/\mu\text{m}^2$ . Since the spot size of the laser is larger than  $10 \mu\text{m}^2$  we would not be able to resolve single quantum dots without spatial filtering. For this purpose a gold mask with holes of  $10^4 \mu\text{m}^2$  aperture was placed on the sample.

## 2.3 Three path set-up

Once a source ready, we send the signal beam (or one of the signals for the HSPS) coming from it which then goes into the three path set-up to evaluate each of the constituent of the second order interference term. It is prepared along the path to go in the interferometer part which will then by moving the shutters provide every combination. The collected intensity at the output of the system will be used to calculate the  $\kappa$  value.

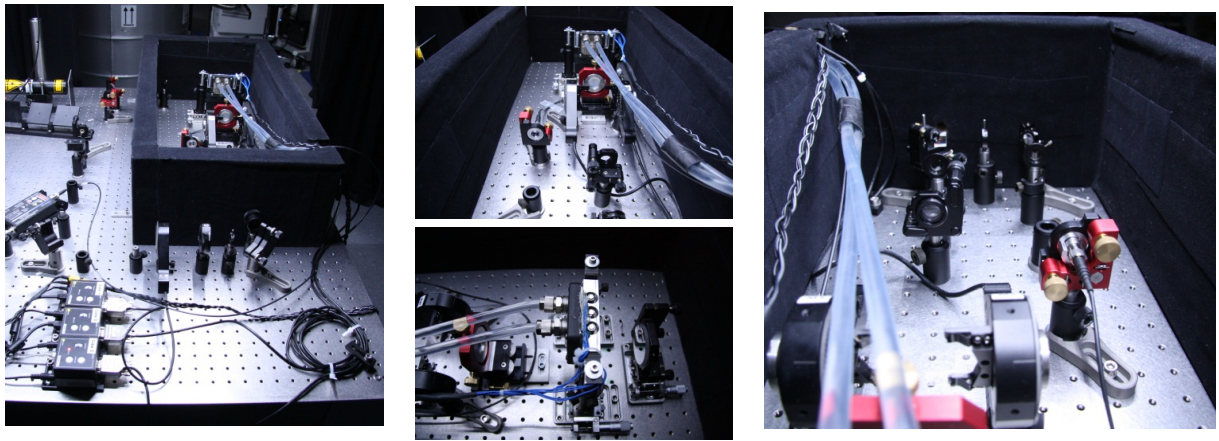


Figure 2.15: Photographies du montage à trois fentes

All the components are directly screwed on the optical table to be the most stable possible as we want to conduct measurements during several days. An isolation box is put around the interferometer part to prevent air movement distortions. The isolation box is made of wood with polystyrene interior and is covered in black velvet. A thick black curtain also enclosed the concerned part of the optical table to avoid external lighting which increases dark counts. Schematically the three-path set-up can be described as in Figure 2.16.

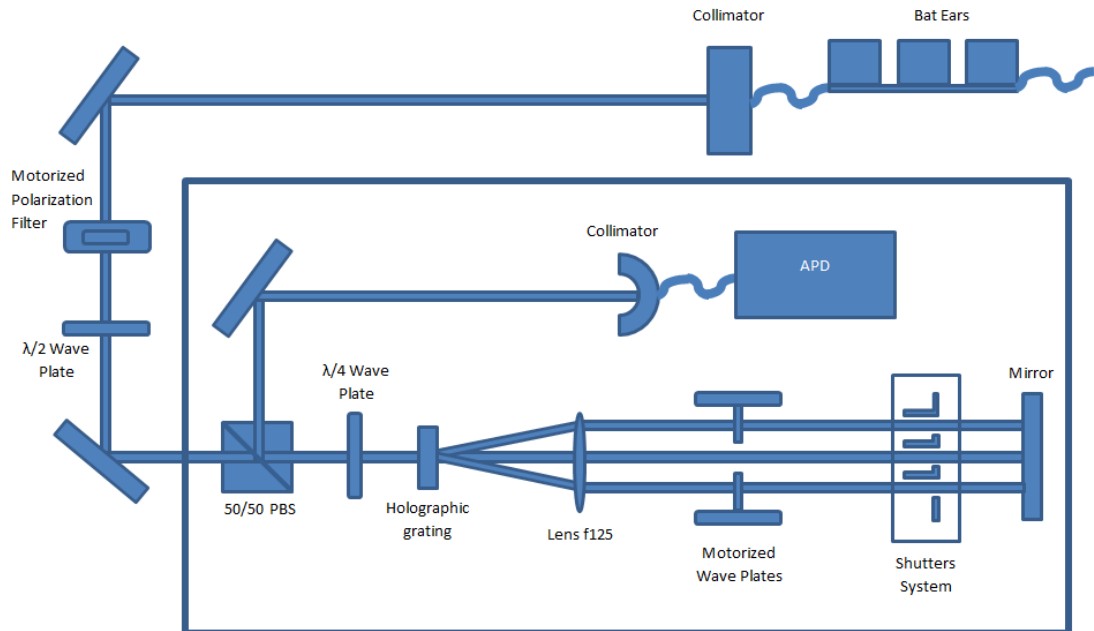


Figure 2.16: Schéma du montage à trois fentes

First we send the signal beam from the source through bat ears to have control over its polarization state before it goes into the interferometer. On the way it goes in a motorized polarization filter which can be moved by the computer to modulate the intensity coming into the set-up. Then it goes through a half wave plate to rotate the polarization of the beam before the box. Even if it goes through bat ears before being emitted by the first collimator it is very important that the beam is horizontally polarized as we will see later, indeed the polarization can slightly rotate over the way or when it is reflected on the mirrors.

Inside the box it goes into a PBS, the reflected part of the beam at the entry of the box must be minimized as much as possible (by acting on the first wave plate) to have the maximum incident intensity to interfere with. Then it goes a first time into the quarter wave plate and is split by a holographic grating. The beam is split in five main parts which continue onto a lens to collimate three of the five resultant beams (the two exterior ones are reflected on the mount of the lens). The lens is placed at the middle between the grating and the mirror, each one being one focal length away for these parts to form a  $4f$  reflection system. Two of the beams go through a motorized phase plate to be able to control the interferences and find the maximum when performing the phase correction. The three beams pass through the shutters system and are reflected by the flat mirror to do the same path back and be refocused by the holographic grating.

Finally it goes a second time through the quarter wave plate. Its polarization is now reversed compared to the incoming beam so that it will be this time reflected by the PBS to be collected by a detector which is connected to the other APD (other channel).

## 2.4 Slits systems

The function of the shutters is to provide each of the eight possible combinations of the three paths. These combination are the eight terms of  $I_{ABC}^2$  that we will use to calculate  $\kappa$ . In the previous work with three-slits experiment [6] a mask with every combination was used. The disadvantage using a mask is that if one of the combinations of the mask is not perfect, a systematic error comes in. Note that if this error is known it is easy to compensate. Due to the higher distances of the paths compared to the shutters, these shutters can be made bigger for a system to be developed which can shut every beam individually. We tested only one of such system but while conducting this study we started the development of two new designs.

### 2.4.1 System used

The system we used was already there when I arrived. It is made from three motors closing and opening vertically three apertures. The shutting devices are linear solenoids consisting of a coil which acts as an electromagnet, and by driving a current, a ferromagnetic core is pulled into the coil. Small flags mounted on the top of the core block the paths when the current flows.

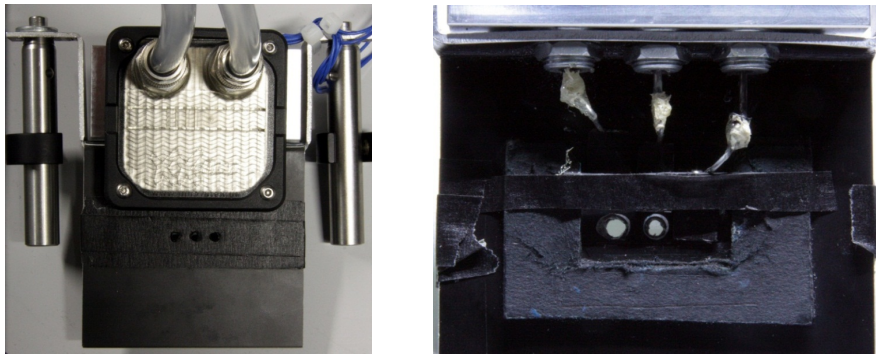


Figure 2.17: Photographies du système de fentes

While the paths are blocked the coils have to be driven by current. Every beam is blocked half of the time. The solenoids have a power consumption of 4 W, also every coil convert a power of 2 W into heat. That make the interferometer emit an overall heat power of 6 W. Without any intervention the shutters are heated up to several tens of degrees. That distorts the phase in the interferometer by air convection and induces a change of the refractive index that perturb the measurement.

This is why water based cooling going around the motors was implemented. To cool the system the coils are mounted into a block of aluminium, which is actively cooled by a CPU water cooling system. Since such systems are made for cooling power of a few 10 W, it can keep the temperature constant at room temperature. Figure 2.17 shows photographs of the shutters. The shutters are controlled by the control software via a driving circuit and the USB 4303 Box which is the same device used for the coincidences counter.

The system had to be improved as it is pretty slow, big, and heavy and the water cooling had to be dropped. Moreover core movements inside the coils to open and close the shutters were too hard and the set-up needed several ms for the optical table to absorb the vibrations. This is why we thought of new versions to be tested.

## 2.4.2 The new designs

We thought about some new systems which would overcome the previously mentioned limitations. There are currently two main proposals for such a system.

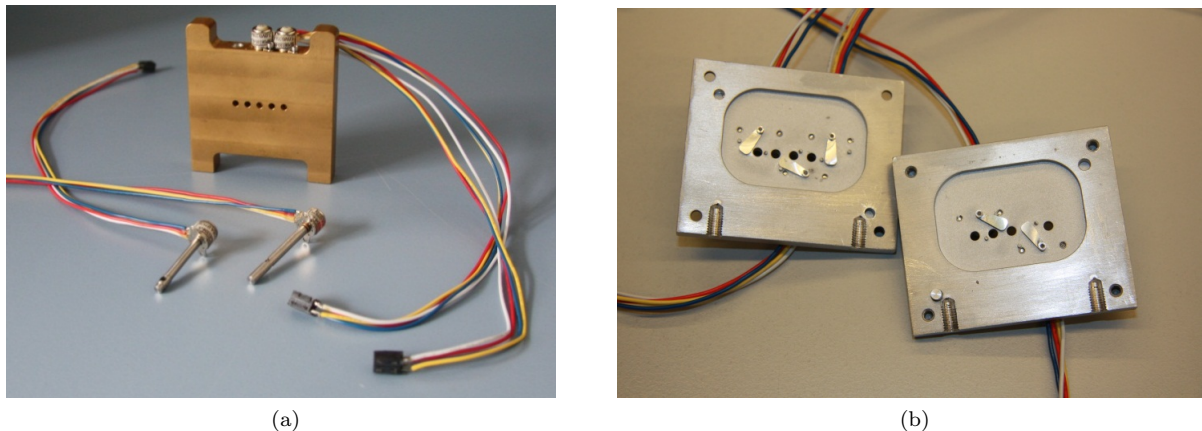


Figure 2.18: Photographies des deux systèmes actuellement réalisés

The first one (Figure 2.18a) is composed of poles that are glued on stepper motors axes as you can see in the center of the picture. These motors are from Nanotec (data sheet can be found at [de.nanotec.com/downloads/A.pdf](http://de.nanotec.com/downloads/A.pdf)) and are screwed on the structure, inserted in holes. They are three motors on top and two screwed at the bottom, with poles looking up, to provide minimal spacing between the shutters. By rotating in their holes those poles open or close the shutter by presenting or not an aperture. The main problem was that the poles were not completely vertically and centrally glued on the axes so that after some testing, with the friction in the holes, they got stuck and that sometimes for numerous numbers of steps in the same position leading to an incomplete closing or opening of the slit. This is why an improved version of the pole (left motor in the picture) was made with the poles only at the size of the hole around the aperture and the hole smaller under it so that the friction is limited and the verticality improved.

The second version (Figure 2.18b) has the motors directly attached to the sides of the structure. The stepper motors are also positioned as three at the upper side of the shutters and two under but this time mixed in order between the faces. Axes of the motors make little ear pieces move and they either hide or discover the slit's apertures from the inside of the structure. The movement is not in the same direction and it is an alternative to the tubes gluing problem. But there are two main problems in this approach. The first problem is that the apertures of the slits are all connected by free space inside the structure so there can be scattering on the inside leading to light coming from closed shutters.

The second one is that, as the motors being attached on the faces, it takes more space in a practical optical set-up and as they are not far away from shatters apertures they also make the alignment of the set-up trickier and can even also induce scattering. The disposition of the motors connection cable is also to take into account.

Due to all the limitations of the second shatter system we decided to pursue further with the first design that we want to improve again. We are currently looking for new motors and also to manufacture the poles in 3D printing of polymers so that there is less friction in the holes. All connection points between the parts are studied because there are the limit point of the design.

### 2.4.3 Motor driver circuit

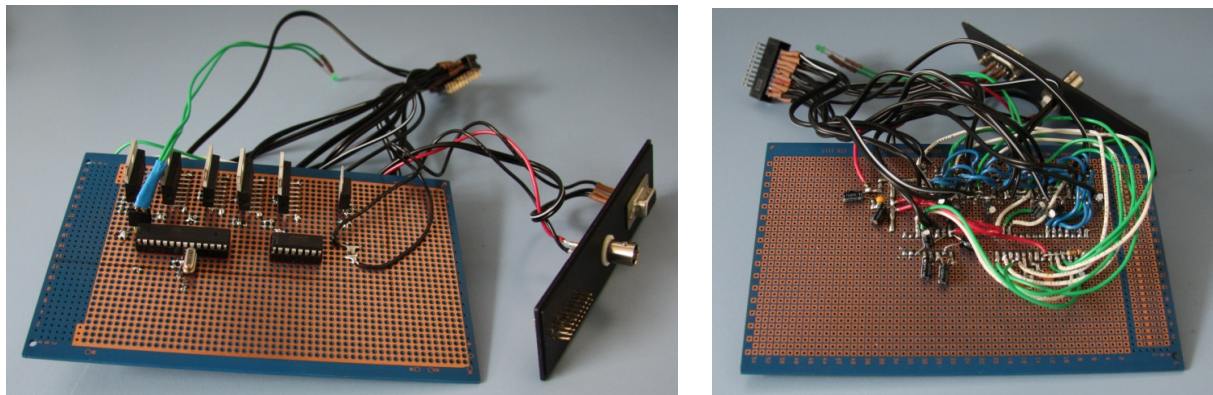


Figure 2.19: Photographies du circuit de contrôle des fentes

The new motors as previously said are stepper motors, they have a step size of  $18^\circ$  so one need to make 20 steps for a  $360^\circ$  revolution of the axis. To move them we build a stepper motor driver circuit based on a microcontroller (MCU). The circuit is alimented via a 5V regulator and its schematics can be found in Appendix C.2. It is quite easy to give instruction to the MCU (another TTL device) through a serial port. The stepper motors are bipolar and are connected to the MCU through a L298 IC bridge circuit with the following available motor sequences:

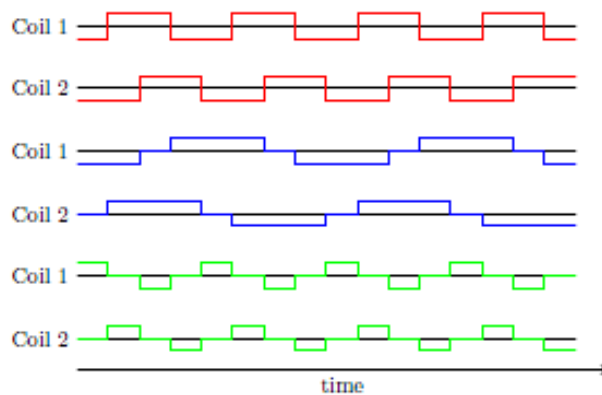


Figure 2.20: Schéma des différentes séquences de mouvement des moteurs en fonction du signal entrant (rouge carré, bleu demi carré et vert sinusoïdale) selon que le voltage soit positif (coil 1) ou négatif (coil 2)

To access the MCU one can use Matlab or Python for example:

```
Matlab – port = serial('COM1')
Python – port = Serial(0, 9600, timeout=0.2)
```

And then access some function of the driver. The system is running an infinite loop, waiting for instructions, once a byte is received it performs an operation according to its value. Some of the main actions of the circuit are:

- Move the motor
- Read motor position
- Set motor speed
- Blink an LED for debugging

To execute a command the user has to call one of the functions by its code letter and then type all the required parameters of the function separated by a separation letter 'N' which also indicates that the instruction string is terminated, all time values are in  $\mu\text{m}$ . Typical Matlab and python calls would look like:

```
Matlab – fprintf(port, call)
Python – port.write(call)
```

Function	Code	Example of call	Description
Move	'M'	'M200N2N1N'	Moves the 2nd motor by 200 steps (10 revolutions) in full stepping (1 to 3 for the drive mode as in fig.)
Move_Delay	'D'	'D200N2N1N1000N2000N3000N4000N5000N5000N4000N3000N2000N1000N'	Same as before but this time add time in $\mu\text{s}$ between each of the 10 revolutions
Set_Delay	'SD'	'SD5000N'	Set the speed of the stepper motors by adding a delay (here 5 ms) between each step
Set_Pause	'SP'	'SP1000N'	Set the pause time between each step here 1 ms (default value)
Return_Delay	'ED'	'ED'	Read and return the speed of the motors, the delay between 2 steps in $\mu\text{s}$ ex: 5000N
Return_Pause	'EP'	'EP'	Read and return the the pause time between 2 steps ex: 5000N for 5 ms
Set_Position	'PS'	'PS2N'	Set the 2nd motor position to $0^\circ$ the origin
Return_Position	'PR'	'PR2N'	Read and return the 2nd motor position ex: 1234N
Abort	'A'	'A'	Abort the current motor operation

Blink	'B'	'B4N'	Make the LED blink twice (2 on 2 off)
Version	'V'	'V'	Returns the current version number of the firmware loaded onto the MCU
Identify	'T'	'T'	Return an identifier contained in the header file terminated by an '\0': 'THREESLIT\0'
Reboot	'R'	'R'	Reboot the MCU

Table 2.1: Appels possibles au driver et leurs descriptions

#### 2.4.4 Testing the new systems

To test those new shatters systems we wrote a python program which combines image processing and electronic control in order to close or open the slits while testing if they do not stop or miss steps.

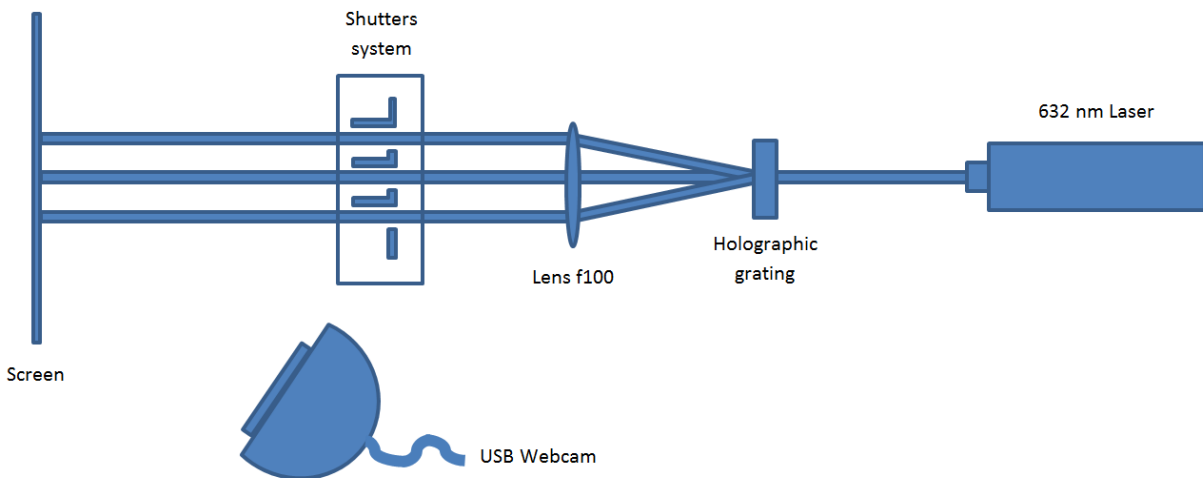


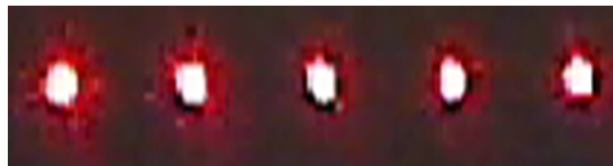
Figure 2.21: Schéma du test des nouveaux systèmes de fentes

The experimental set-up of the test that is drawn schematically in Figure 2.21 consists of a 632 nm laser shooting at an holographic grating to split the beam. The split beam goes then onto a lens to be collimated before going through the shutters system. After the slits there is a screen which is made of some dark, mat tape on a metal plate. An USB web-cam record images from the spots as they are displayed on the screen and feed them to the computer to be analysed by performing image processing in a Python program which is presented in Appendix B.2.

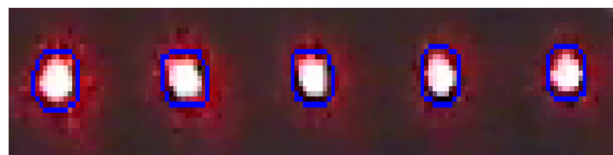
During the test the shutters are moved through all of the combinations randomly and that to see if there is any problem during long time measures. Firstly the program opens a window containing the live feed and waits for the user to select a region of interest (ROI). The selection of the ROI decreases the computation intensity and generally removes all false detections. The shutters at this point should be all open as we will check the area of the brightest pixels in order to set position and surface references to check for problems. A problem will be detected as spots with a different size as the reference ones, a closed slit will be determined by discarding all remaining spots by their positions.

Once the selection of the ROI done, the program makes a quick color selection using thresholds on gray images looking for the brightest pixels which would be spots. It then performs smoothing and dilatation to connect most of the pixels that have passed the threshold test and uses spatial moments determination to evaluate how many areas were detected. The pixels created by the dilatation process are used to highlight the spots by being displayed in blue as one can see on Figure 2.22.

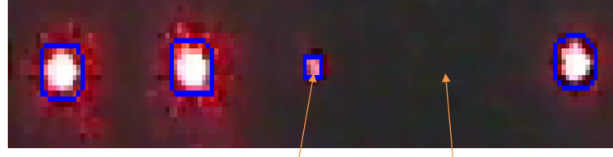
Finally the program calculates the area of the spots detected and checks for each of them if it has moved since the previous frame. If the area is 20% bigger or smaller it updates the corresponding slit state from "Opened" to "Problem". If there is one or more area(s) missing it checks the remaining areas  $x$  positions in pixels and compare them with the positions of the reference spots to find which slits are closed and updates their states to "Closed".



(a) Region Of Interest - ROI



(b) Détection des spots de référence



(c) Evaluation du test

Figure 2.22: Déroulement du processus de test une fois le ROI sélectionné

If needed we could also write every problem events into a file with their discrepancies in area, the time it happened, the duration of the problem or any other useful information to evaluate the quality of the shutter system.

## 3 Results

Once everything implemented we did some measurements with an 808 nm continuous wave laser to assure ourselves that everything was working and then we performed the first measures with the HSPS source. Finally we tried with the quantum dot source. The code used for the calculations is given in Appendix B.3.

### 3.1 Laser

The laser source being stable we can measure for long period of time. Therefore in order to determine the  $\kappa$  value we record 1000 intensity points for each of the eight slits combinations and then we calculate the mean  $\kappa$  value for those 1000 points that will make 1 kappa value to absorb deviations. The kappas calculated according to the equation 1.7. Figure 3.1 shows a measurement where 50 sets of data were taken with random intensity changes between them.

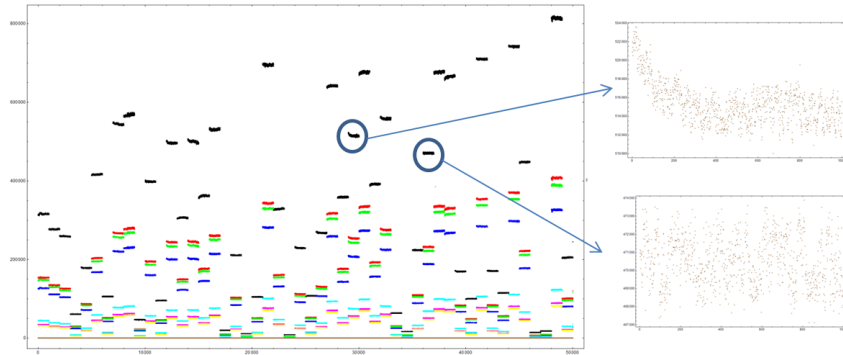


Figure 3.1: Résultats expérimentaux avec le laser à 808 nm

But we can also see in Figure 3.1 that some of the sets are distorted, this is due to the motorized phase filter which controls the intensity. The motor was a bit loses and tended to move after severe intensity changes. This problem is now resolved.

We conducted three measurements with the laser source the results are summarized in Table 3.1 and the plot of the results can be found in Appendix A.1.

	Raw $\kappa$ and standard deviation	n° of points
n°1	$1.310.10^{-2} \pm 2.707.10^{-3}$	6574
n°2	$1.293.10^{-3} \pm 7.466.10^{-4}$	30683
n°3	$1.123.10^{-2} \pm 5.616.10^{-5}$	50182

Table 3.1:  $\kappa$  moyens mesurés avec le laser à 808 nm

The first thing that we can remark is that as the number of points increases the standard deviation decreases accordingly. This is important because the kappa distribution has a Gaussian behavior that is why the longer we measure the better the estimation of the mean value. The second thing is that as the distance between combinations intensity decreases, the kappa distribution spread (see Figure 3.2).

The third remark that one can express is that sometimes one shatter did not closed properly leading to an outsider point that increase the corresponding kappa (Figure 3.3). To remove them one can check for point having a real deviation over 4. Figure 3.4 shows the effect of removing the lowest intensities and the false detection due to shatters malfunction upon  $\kappa$  distribution. Another interesting observation is that there is an asymmetry toward the positive side in the  $\kappa$  distribution, this seemed to be to be due to the fact that high intensities tends to bring the kappas to the negative side while low intensities bring them to the positive side (Figure 3.5). As there are more low intensities data sets the distribution is drifted toward the positives.

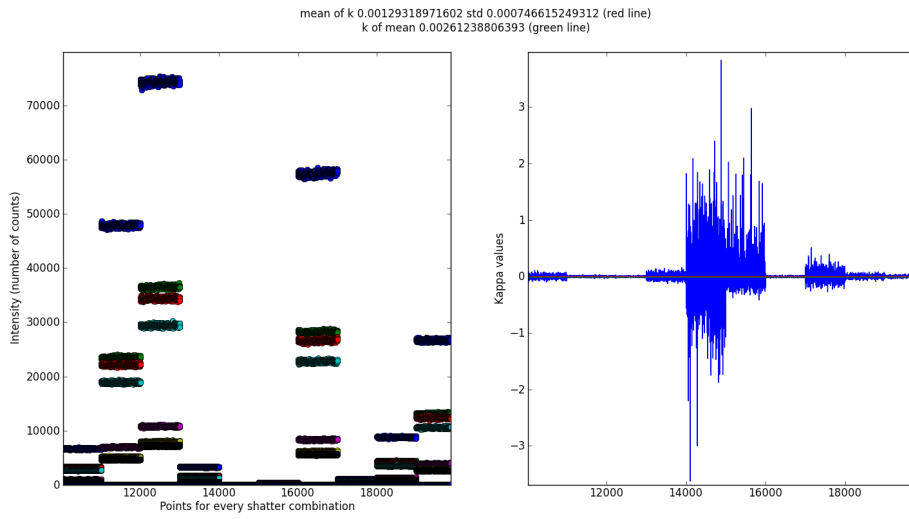


Figure 3.2: Etude de l'effet des variations d'intensité sur la répartition des  $\kappa$

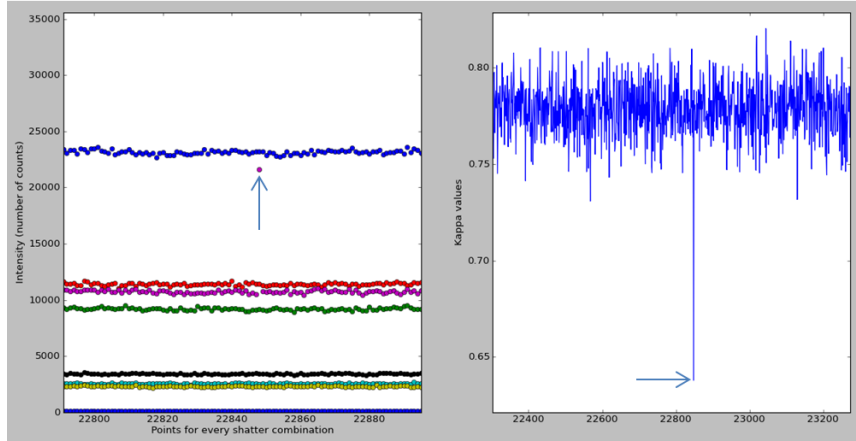


Figure 3.3: Effet d'une erreur de fermeture d'une fente sur le  $\kappa$  correspondant (test n°2)

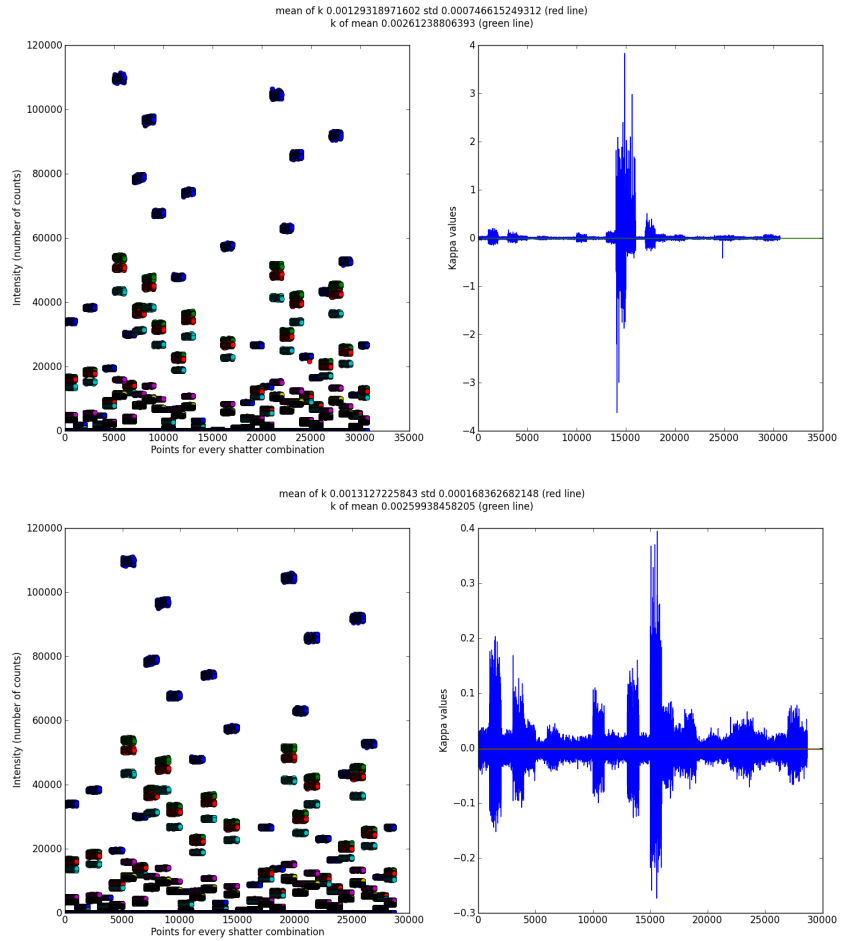


Figure 3.4: Comparaison entre les résultats bruts du test n°2 et ceux une fois les points de trop faible intensité ( $P_{ABC} < 600$ ) et ceux deviant de plus de 4 fois la deviation réelle enlevée

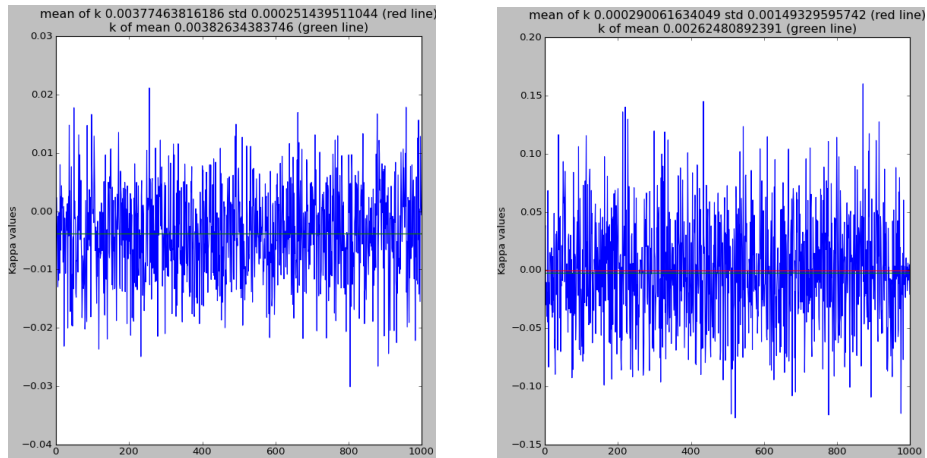


Figure 3.5: Comparaison entre des résultats du test n°2 pour le set 19000-20000 (environ 105000 d'intensité maximale) et le set 13000-14000 (environ 14000 d'intensité maximale)

Note that for the measurements using a laser source these  $\kappa$  can be further reduced by a factor of about 3 to 10 after detector non-linearity compensation [6].

### 3.2 Heralded Single-Photons Source

The first measurement that we did with the source was when the PBS was still in place of the polarizer (Figure 3.6). We measured during the night and gathered a bit more than 6000 points for each of the slits combinations. We have then conducted two more tests to assure the proper working state of the experimental set-up.

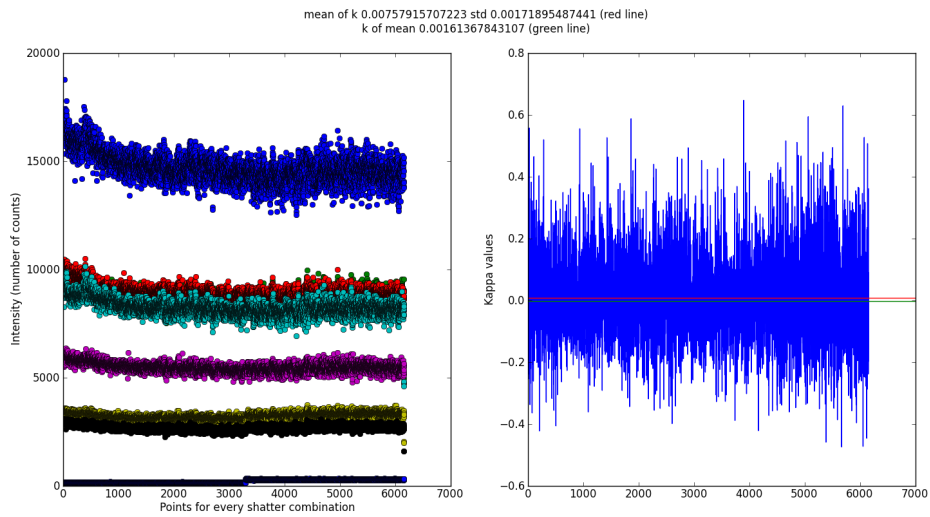


Figure 3.6: Résultat du calcul des kappas de la première mesure

The power decreases exponentially because of three effects, one is that the PBS had some transparency problem as expressed in 2.1.3. The other one is that normally the program does a phase correction to counterbalance temperature distortions as introduced before which have a direct impact on the intensity (Figure 3.7). But as this function does not seem to work anymore, this problem is currently under resolution. But the main problem is that the polarization slightly drifts inside the source, this is probably due to the fibers that connect the input laser, the source and the interferometer. As the beam polarization changes so does the fraction of photons that goes in the arm that runs to the three-paths set-up. Figure 3.8 shows the intensity growing in the second arm that serves for coincidence reference. To conduct longer measurements one has therefore to readjust the polarization while measuring like for the quantum dot source as we will see later. Plots of the results are again available in Appendix A.2 and the mean  $\kappa$  values are presented in Table 3.2.

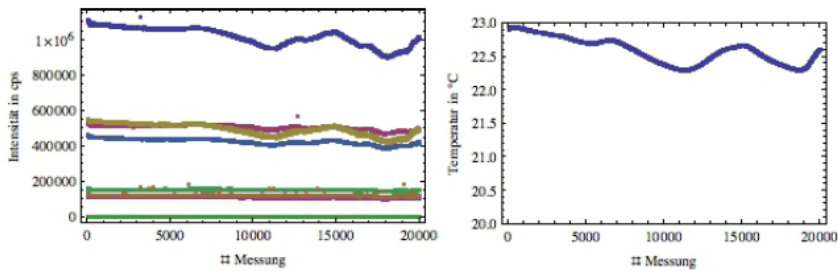


Figure 3.7: Corrélation entre intensité mesurée par les détecteurs et température

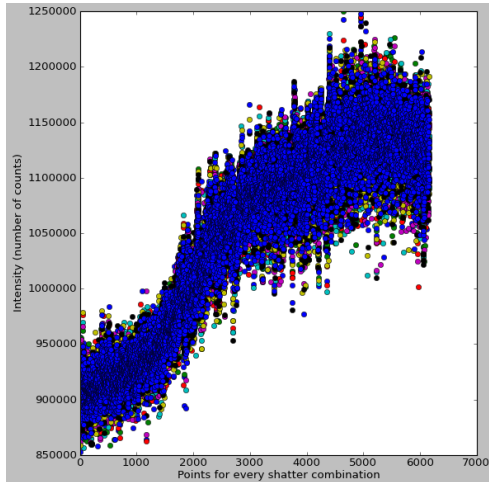


Figure 3.8: Augmentation de l'intensité lumineuse dans le deuxième bras due au changement de polarisation

	Raw $\kappa$ and standard deviation	n° of points
n°1	$1.614 \cdot 10^{-3} \pm 1.719 \cdot 10^{-3}$	6155
n°2	$1.164 \cdot 10^{-2} \pm 2.909 \cdot 10^{-3}$	18896
n°2 corrected	$1.165 \cdot 10^{-2} \pm 2.598 \cdot 10^{-3}$	15875
n°3 corrected	$1.010 \cdot 10^{-3} \pm 5.021 \cdot 10^{-3}$	4504 (5013 full)

Table 3.2:  $\kappa$  moyens mesurés avec la source HSPS

The second and third measures that we conducted with the polarizer also present the effect of the polarization changes but the laser shut down in during the experiment as one can see on the figures and that has severely impacted the  $\kappa$ . For those results we used the same kind of threshold upon the data as the one used to reduce the kappas distribution through low intensities removing for the laser.

There are still a handful of improvements to make in order to go beneath the laser's  $\kappa$  value as expected by the theory. It is still needed to conduct more optimized and long measurements with this source as I ran out of time. We also expected good results with the quantum dot source for which we had to rebuild the three-path setup as its emission is at 918 nm.

### 3.3 Quantum dot

We performed only a single measurement with the quantum dot source as we had a shortage in helium that has frozen all manipulations. The result for the raw data is presented in Figure 3.9.

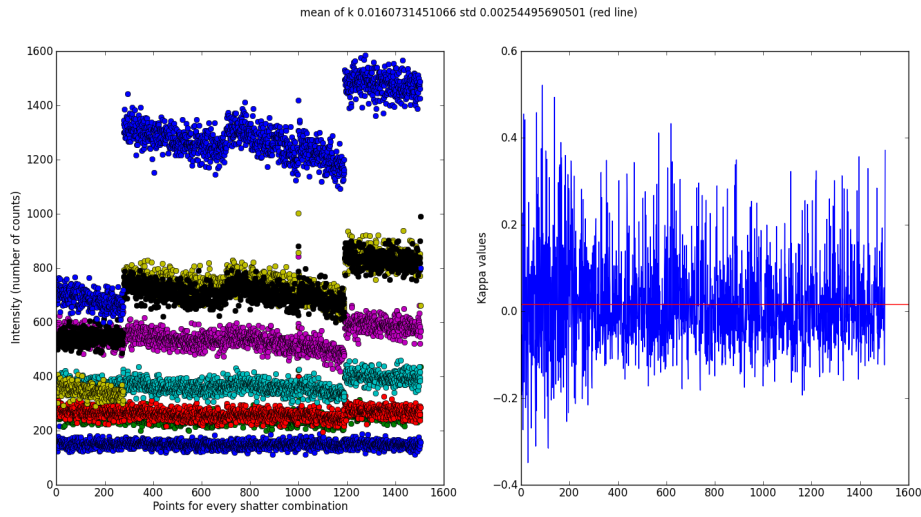


Figure 3.9: Résultats expérimentaux avec la source de boîte quantique

We can see in Figure 3.9 that the first part (points 1-277) is not so good, this is due to the the fact that we were not at the maximum of interference at the beginning of the measure. Figure 3.10 shows the results discarding those points.

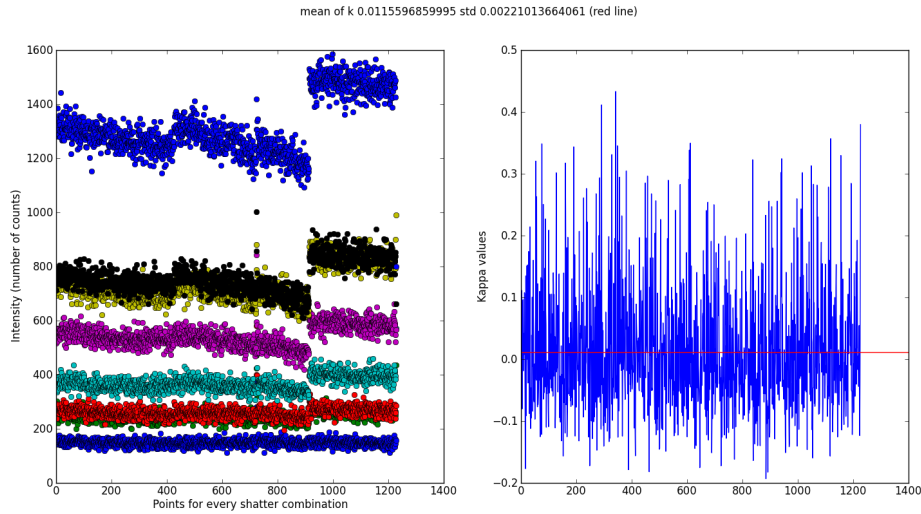


Figure 3.10: Résultats expérimentaux après avoir enlevé les 277 premiers points

There are three different sets remaining this is because the excitation of the dot had to be readjusted as it drifts slowly away with time. Results for the overall measurements and for each sets are shown in Table 3.3. Again some plots are available in appendix (A.3).

	Raw $\kappa$ and standard deviation	n° of points
overall points	$1.607.10^{-2} \pm 2.545.10^{-3}$	1505
3 sets	$1.156.10^{-2} \pm 2.210.10^{-3}$	1228
two firsts	$1.046.10^{-2} \pm 3.134.10^{-3}$	906
first	$1.780.10^{-2} \pm 3.286.10^{-3}$	420
second	$4.121.10^{-3} \pm 2.983.10^{-3}$	486
third	$1.321.10^{-2} \pm 3.036.10^{-5}$	322

Table 3.3:  $\kappa$  moyens mesurés avec la source de boîte quantique

The better set is the second one, the overall results are a bit worth than those obtained with the HSPS source but once again this is due to the fact that the intensities have a lower amplitude. Even if it induces a smaller distribution it also drifts this distribution toward the positives, maybe with a better optimization of the set-up (emission, light transport between the source and the interferometer, collimation in general,...) we could find an appropriate compromise for this experiment to bring the  $\kappa$  distribution centered as close as possible to zero. In addition the source needing to be readjusted every hour or so it is impossible to conduct a measurement over a week to have more  $\kappa$  for better homogeneity and accuracy.

### 3.4 Quaternion criterion

To conclude this study we calculated the criterion  $F(\alpha, \beta, \gamma)$  from Peres alongside our measurements. We adapted the formulation to match our experiment (equation 1.11) and the results are shown in Table 3.4 next to the kappas for comparison. For reminder  $0 < F < 1$  normally means that quaternionic formulation is admitted but the divergence is probably solely due to experimental errors. Therefore  $F$  is a direct indication of the quality of our experimental installation, the closest  $F$  to 1, the better the experiment.

	Mean $\kappa$ and standard deviation	Peres criterion
Laser	$1.310.10^{-2} \pm 2.707.10^{-3}$	0.880
	$1.293.10^{-3} \pm 7.466.10^{-4}$	0.934
	$1.123.10^{-2} \pm 5.616.10^{-5}$	0.957
HSPS	$1.614.10^{-3} \pm 1.719.10^{-3}$	0.901
	$1.164.10^{-2} \pm 2.909.10^{-3}$	0.814
	$1.165.10^{-2} \pm 2.598.10^{-3}$	0.873
	$1.010.10^{-3} \pm 5.021.10^{-3}$	0.822

Dot	1.607.10 <sup>-2</sup> ± 2.545.10 <sup>-3</sup>	0.877
	1.156.10 <sup>-2</sup> ± 2.210.10 <sup>-3</sup>	0.894
	1.046.10 <sup>-2</sup> ± 3.134.10 <sup>-3</sup>	0.890
	1.780.10 <sup>-2</sup> ± 3.286.10 <sup>-3</sup>	0.991
	4.121.10 <sup>-3</sup> ± 2.983.10 <sup>-3</sup>	0.889
	1.321.10 <sup>-2</sup> ± 3.036.10 <sup>-5</sup>	0.905

 Table 3.4:  $\kappa$  moyens mesurés avec la source de boîte quantique

Another interesting thing to observe is the correlation between the criterion, the corresponding kappa and its standard deviation. Figure 3.11 shows this correlation.

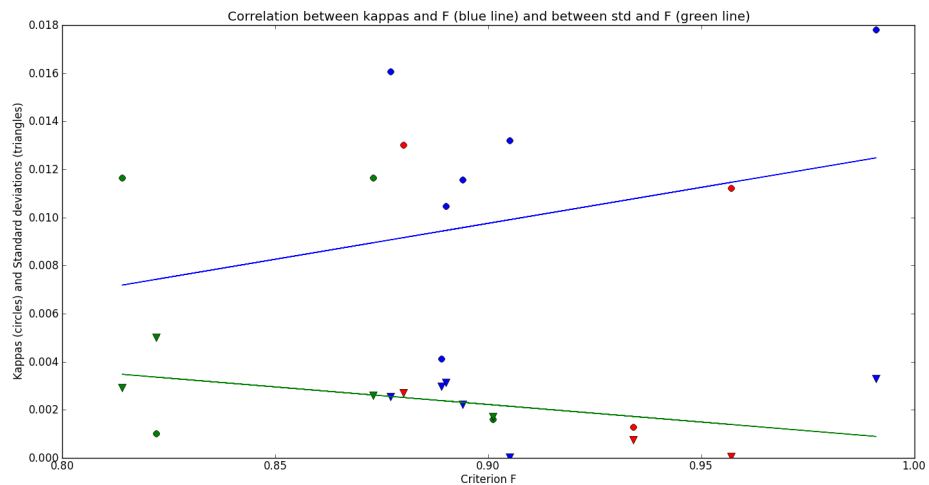


Figure 3.11: Etude de la corrélation entre les résultats des kappas et ceux du critère de Peres. Les marqueurs en rouge sont les points du laser, ceux en vert ceux de la source HSPS et ceux en bleu ceux de la source de la boîte quantique

It seems that this correlation exists as we can see the symmetrical linear behaviors of the kappas and standard deviations with the quaternionic criterion. The kappas are going toward zero for the criterion diverging from 1 and the standard deviations are going close to zero for the criterion approaching 1. According to Peres interpretation this would indicate that the Born rule would be experimentally proved by taking into account some quaternionic effects. The complex notation ( $F = 1$ ) could describe the experimental system as the deviations are narrowing to zero for high  $F(\alpha, \beta, \gamma)$ . It would be interesting to further investigate this relation between the algebra involved and the statistical interpretation of the wave function.

# Summary

During this internship I had the chance to discover experimental physics. I implemented optical setups, the heralded single-photon source and the three-paths set-up, build hardware, the oven for the crystal with its temperature controller, the coincidence counter, the stepper motors driver and the new shutters systems and software, several python codes to simulate and calculate all the needed parts of phenomenons taking place in the experiment in order to perform data acquisition and processing.

I used three kind of source, a laser source at 808 nm, an heralded single photon source at 808 nm and a quantum dot source at 918 nm to perform the quantum interference experiment in order to probe the Born rule. We tested the quantum experiment with the 808 nm laser and found a best kappa of  $\kappa = 1.293.10^{-3} \pm 7.466.10^{-4}$ . A reduction of the measured  $\kappa$  was expected when using single-photon sources as we know exactly how many photons were emitted. Currently we did not show this behavior in the first measurements that we conducted with our heralded single-photon source as there are still some experimental problems to tackle. The best result we got was  $\kappa = 1.010.10^{-3} \pm 5.021.10^{-4}$  but there was no phase correction and it seemed that there were too few sets for the detector non-linearity compensation method to work. The quantum dot source gave  $\kappa = 4.121.10^{-3} \pm 2.983.10^{-3}$ .

The main difference between the single-photons sources and the laser is the measurement time, as the kappas are normally distributed, the kappa value that we find by taking the mean value of this distribution gain in accuracy over the number of kappas in this distribution. That is why the single-photons source are not better than the laser one. The kappa values strongly differs with the last data point acquisition making our results inaccurate. One can wait for the good value to pop out or play with the intensity that impact the distribution to have a nearly perfect result. This is why one need to measure for a long time to smooth this limitation. The single photon sources are not very stable with time the smoothing of the kappa distribution will be difficult with them. To further improve the experiment one could also try to reduce further the experimental errors along the set-up. It would also be interesting to test one of the new shutters systems and implement the three-paths set-up in transmission as well.

An intriguing results comes from the study of the quaternionic effect criterion from Peres that we calculated with our set-up. It suggests that if the experimental system can be modeled using complexes, our criterion to test the Born's rule representing the complex statistical interpretation of the wave function seems to indicate the need to include some quaternionic effects that are at play in our calculus. But this can also be an experimental artifact.

## Bibliography

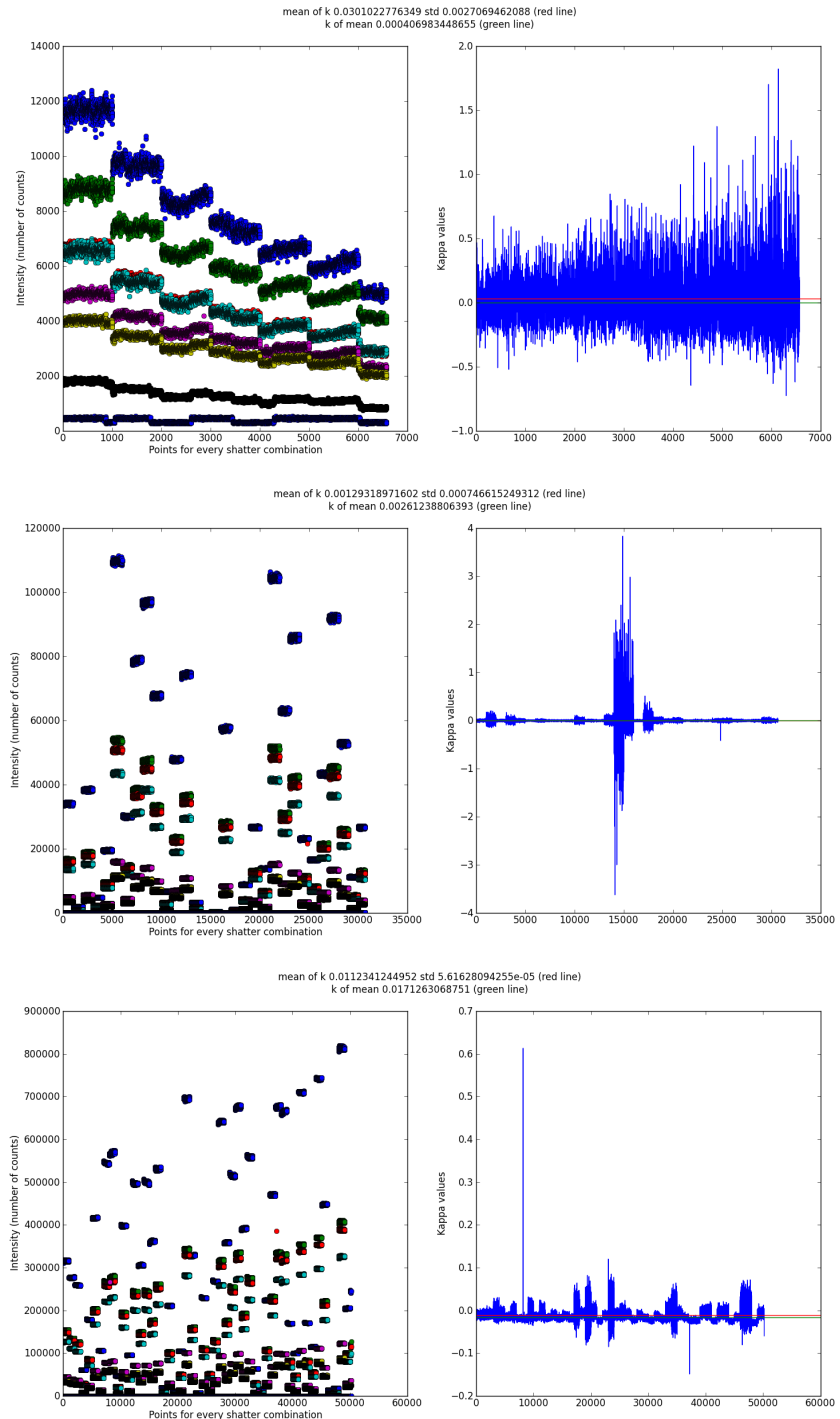
- [1] T. Young, “Experiments and calculations relative to physical optics (the 1803 bakerian lecture),” *Philosophical Transactions of the Royal Society of London*, pp. 1–16, 1994.
- [2] C. Jönsson *Zeitschrift für Physik*, vol. 161, pp. 454–474, 1961.
- [3] R. Sorkin, “Quantum mechanics as quantum measure theory,” *Modern Physics Letters A*, vol. 9, pp. 3119–3127, 1994.
- [4] W. Wootters, “Quantum mechanics without probability amplitudes,” *Foundations of Physics*, vol. 16, pp. 391–405, 1986.
- [5] U. Sinha, C. Couteau, T. Jennewein, R. Laflamme, and G. Weihs, “Ruling out multi-order interference in quantum mechanics,” *Science*, vol. 329, no. 5990, pp. 418–421, 2010.
- [6] I. Söllner, B. Gschösser, P. Mai, B. Pressl, Z. Vörös, and G. Weihs, “Testing born’s rule in quantum mechanics for three mutually exclusive events,” *Foundations of Physics*, pp. 742–751, 2012.
- [7] M. Born, “Zur Quantenmechanik der Stoßvorgänge,” *Zeitschrift für Physik*, vol. 37, pp. 863–867, Dec. 1926.
- [8] M. Born, “Quantenmechanik der Stoßvorgänge,” *Zeitschrift für Physik*, vol. 38, pp. 803–827, Nov. 1926.
- [9] A. Pais, “Max born’s statistical interpretation of quantum mechanics,” *Science*, vol. 218, no. 4578, pp. 1193–1198, 1982.
- [10] E. Schrödinger, “An undulatory theory of the mechanics of atoms and molecules,” *Phys. Rev.*, vol. 28, pp. 1049–1070, Dec 1926.
- [11] R. Sorkin, “Quantum measure theory and its interpretation,” *ArXiv General Relativity and Quantum Cosmology e-prints*, July 1995.
- [12] A. Kolmogorov, “Foundations of the theory of probability (2nd ed.),” New York: Chelsea, 1956.
- [13] A. Peres, “Proposed test for complex versus quaternion quantum theory,” *Phys. Rev. Lett.*, vol. 42, pp. 683–686, Mar 1979.
- [14] W. R. Hamilton, “On quaternions; or on a new system of imaginaries in algebra,” *letter to John T. Graves*, 1843.
- [15] A. Hurwitz, “On the composition of quadratic forms of arbitrary many variables. (ueber die composition der quadratischen formen von beliebig vielen variabeln.),” 1898.
- [16] B. Saleh and M. Teich, “Fundamentals of photonics,” John Wiley & Sons, 2007.
- [17] A. Mosset, F. Devaux, G. Fanjoux, and E. Lantz, “Direct experimental characterization of the bose-einstein distribution of spatial fluctuations of spontaneous parametric down-conversion,” *Eur. Phys. J. D*, vol. 28, no. 3, pp. 447–451, 2004.
- [18] D. Meschede, “Optics, light and lasers,” Wiley-VCH, 2007.
- [19] M. M. Fejer, G. A. Magel, D. H. Jundt, and R. L. Byer, “Quasi-phase-matched second harmonic generation: Tuning and tolerances,” *IEEE J. Quantum Electron.*, vol. 28, pp. 2631–2654, nov 1992.
- [20] V. Berger, A. Fiore, E. Rosenthaler, P. Bravetti, and J. Nagle, “Phase matching using an isotropic non linear optical material,” *Nature*, vol. 391, p. 463–466, 1998.

- [21] W. P. Risk, T. R. Gosnell, and A. V. Nurmikko, “Compact blue-green lasers,” Cambridge University Press, 2003.
- [22] H. Vanherzeele, J. D. Bierlein, and F. C. Zumsteg, “Index of refraction measurements and parametric generation in hydrothermally grown  $ktiopo_4$ ,” *Appl. Opt.*, vol. 27, pp. 3314–3316, Aug 1988.
- [23] J. A. Armstrong, N. Bloembergen, J. Ducuing, and P. S. Pershan, “Interactions between light waves in a nonlinear dielectric,” *Phys. Rev.*, vol. 127, pp. 1918–1939, Sep 1962.
- [24] G. D. Boyd and D. A. Kleinman, “Parametric Interaction of Focused Gaussian Light Beams,” *Journal of Applied Physics*, vol. 39, pp. 3597–3639, July 1968.
- [25] P. Ramazza, S. Ducci, A. Zavatta, M. Bellini, and F. Arecchi, “Second-harmonic generation from a picosecond ti:sa laser in lbo: conversion efficiency and spatial properties,” *Applied Physics B: Lasers and Optics*, vol. 75, pp. 53–58, 2002.
- [26] Y. Chen and Y. Chen, “Analytical functions for the optimization of second-harmonic generation and parametric generation by focused gaussian beams,” *Applied Physics B: Lasers and Optics*, vol. 76, pp. 645–647, 2003.
- [27] O. Stier, M. Grundmann, and D. Bimberg, “Electronic and optical properties of strained quantum dots modeled by 8-band k-p theory,” *Phys. Rev. B*, vol. 59, pp. 5688–5701, Feb 1999.
- [28] G. Medeiros-Ribeiro, F. G. Pikus, P. M. Petroff, and A. L. Efros, “Single-electron charging and coulomb interaction in inas self-assembled quantum dot arrays,” *Phys. Rev. B*, vol. 55, pp. 1568–1573, Jan 1997.
- [29] U. Banin, Y. Cao, D. Katz, and O. Millo, “Identification of atomic-like electronic states in indium arsenide nanocrystal quantum dots,” *Nature*, vol. 400, pp. 542–544, Aug 1999.
- [30] J. Shumway, A. Franceschetti, , and A. Zunger, “Correlation versus mean-field contributions to excitons, multiexcitons, and charging energies in semiconductor quantum dots,” *Phys. Rev. B*, vol. 63, p. 155316, Mar 2001.
- [31] E. Moreau, I. Robert, L. Manin, V. T.-M. J. Gerard, and I. Abram, “Quantum cascade of photons in semiconductor quantum dots,” *Phys. Rev. Lett.*, vol. 87, p. 183601, Oct 2001.
- [32] S. Grabher, I. Soellner, A. Predojevic, and G. Weihs, “Pulsed sagnac source of polarisation entangled photon pairs,” *CLEO Europe and EQEC 2011 Conference Digest*, p. EA P2, 2011.
- [33] E. Bocquillon, C. Couteau, M. Razavi, R. Laflamme, and G. Weihs, “Coherence measures for heralded single-photon sources,” *Phys. Rev. A*, vol. 79, p. 035801, Mar 2009.
- [34] M. Razavi, I. Söllner, E. Bocquillon, C. Couteau, R. Laflamme, and G. Weihs, “Characterizing heralded single-photon sources with imperfect measurement devices,” *Journal Of Physics. B, Atomic, Molecular And Optical Physics*, vol. 42, p. 114013, Jan 2009.
- [35] M. T. L. Ouvrad *Compt. Rend.*, vol. 121, p. 117, 1890.
- [36] F. C. Zumsteg, J. D. Bierlein, and T. E. Gier, “ $k_xrb_{1-x}tiopo_4$ : A new nonlinear optical material,” *Journal of Applied Physics*, vol. 47, no. 11, pp. 4980–4985, 1976.
- [37] M. Roth, “Stoichiometry and domain structure of ktp-type nonlinear optical crystals,” in *Springer Handbook of Crystal Growth* (G. Dhanaraj, K. Byrappa, V. Prasad, and M. Dudley, eds.), pp. 691–723, Springer Berlin Heidelberg, 2010.
- [38] M. C. Gupta, W. P. Risk, A. C. G. Nutt, and S. D. Lau, “Domain inversion in  $ktiopo_4$  using electron beam scanning,” *Applied Physics Letters*, vol. 63, pp. 1167 –1169, aug 1993.
- [39] Q. Chen and W. Risk, “Periodic poling of  $ktiopo_4$  using an applied electric field,” *Electronics Letters*, vol. 30, pp. 1516 –1517, sep 1994.

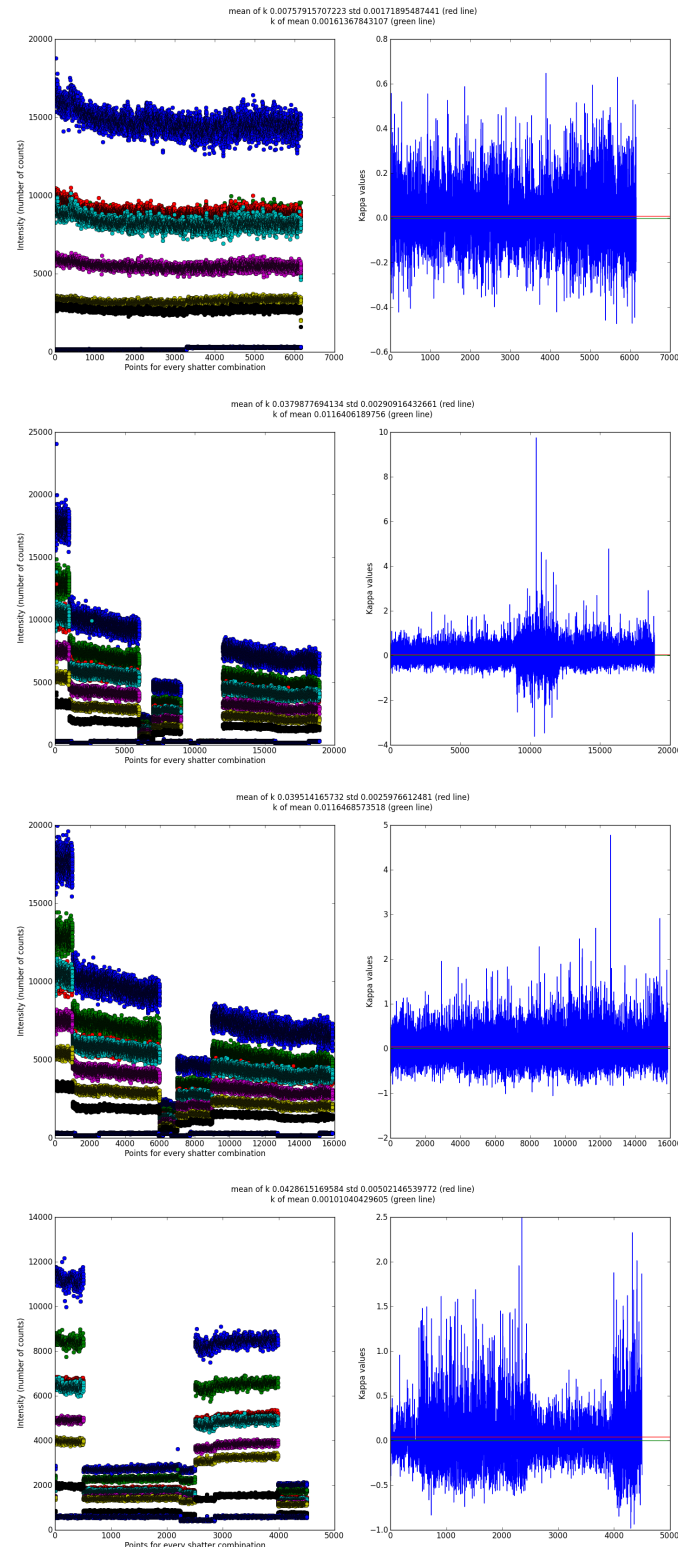
- [40] G. Rosenman, A. Skliar, M. Oron, and M. Katz, "Polarization reversal in ktp crystals," *Journal of Physics D: Applied Physics*, vol. 30, no. 2, p. 277, 1997.
- [41] H. Karlsson and F. Laurell, "Electric field poling of flux grown ktp," *Applied Physics Letters*, vol. 71, pp. 3474–3476, dec 1997.
- [42] K. S. Buritskii, V. A. Chernykh, E. M. Dianov, V. A. Maslov, and E. A. Shcherbakov, "Domain inversion induced by dielectric film cladding in ktp," *Sov. Lightwave Commun*, vol. 3, p. 111–117, 1993.
- [43] H.-A. Bachor and T. C. Ralph. in *A Guide to Experiments in Quantum Optics*, KGWILEY-VCH Verlag GmbH & CoA, Weinheim, 1998.
- [44] P. Michler, "Nonclassical light from single semiconductor quantum dots," in *Single Quantum Dots*, vol. 90 of *Topics in Applied Physics*, pp. 315–347, Springer Berlin / Heidelberg, 2003.
- [45] D. G. Austing, S. Sasaki, S. Tarucha, S. M. Reimann, M. Koskinen, and M. Manninen, "Ellipsoidal deformation of vertical quantum dots," *Phys. Rev. B*, vol. 60, pp. 11514–11523, Oct 1999.
- [46] G. Bryant and G. Solomon, "Optics of quantum dots and wires," Artech House, 2005.
- [47] V. A. Shchukin, N. N. Ledentsov, P. S. Kop'ev, and D. Bimberg, "Spontaneous ordering of arrays of coherent strained islands," *Phys. Rev. Lett.*, vol. 75, pp. 2968–2971, Oct 1995.
- [48] E. H. C. Parker, "The technology and physics of molecular beam epitaxy," New York: Plenum Press, 1985.
- [49] C. M. Santori, *Generation of nonclassical light using semiconductor quantum dots*. PhD thesis, Stanford University, 2003.

# A Results

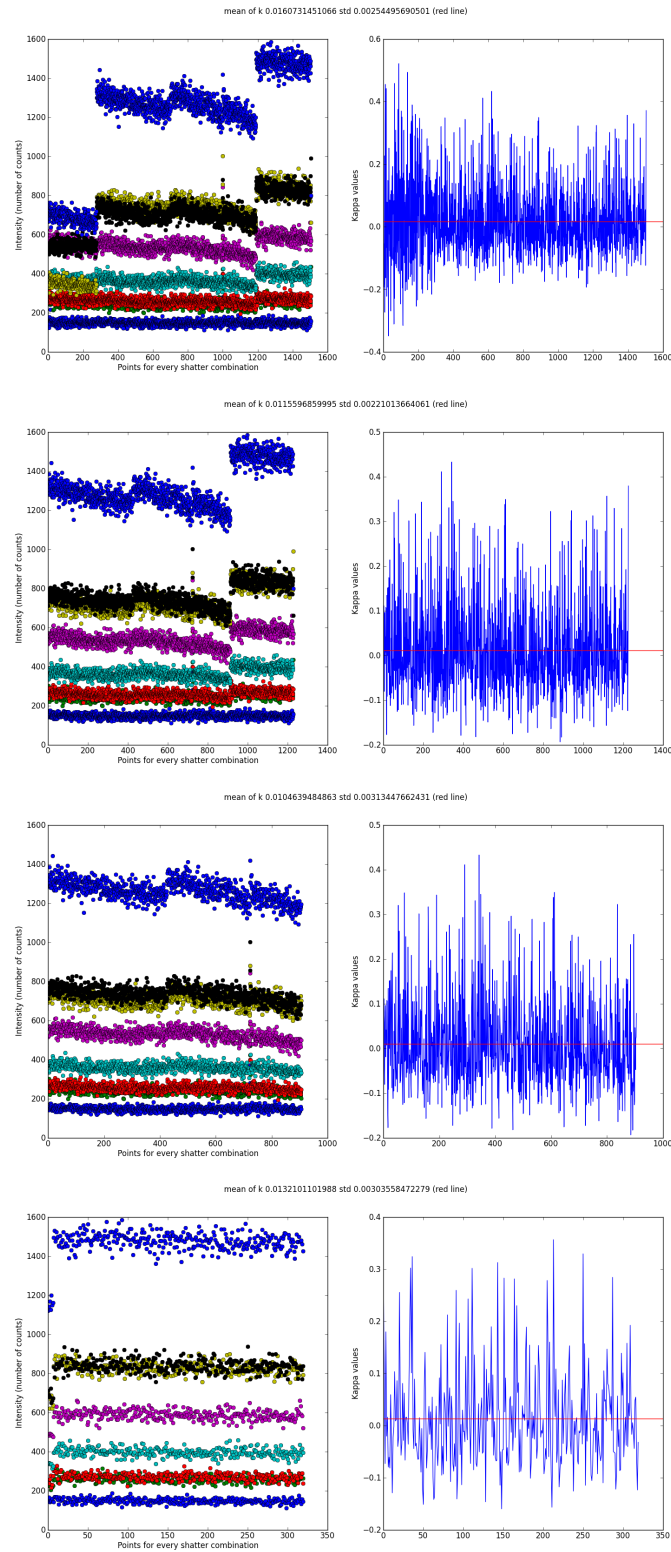
## A.1 Laser



## A.2 Heralded single-photon source



### A.3 Quantum dot source



## B Python codes

### B.1 Two lenses ABCD system

```

from math import sqrt, pi, atan, exp, sin
import cmath
import pylab as pl
import numpy as np

# Little utility function to construct array of floats
def frange(x, y, nb):
    Similar to xrange but for floats : x = start, y = end, nb = number of points
    num = float(y - x) / nb
    while x < y:
        yield x
        x += num
    yield y

#####
def Freespace(d):
    return [[1, float(d)], [0, 1]]

def Lens(f):
    return [[1, 0], [-1 / float(f), 1]]

def invqOptiq(invq, Optiq):
    return (Optiq[1][0] + (Optiq[1][1] * invq)) / (Optiq[0][0] + (Optiq[0][1] * invq))

#####
def woutofq(invq):
    return sqrt((system[0]['lam'] / (-pi * invq.imag)))

def wpos(invq):
    return -invq.real / abs(invq)** 2

def wsize(invq):
    return woutofq(invqOptiq(invq, Freespace(wpos(invq)))))

#####
def beam():
    invq2 = system[0]['invq']
    x, w = {}, {}
    for n in range(len(system) - 1):
        if n > 0:
            invq1 = invqOptiq(invq2, Freespace(system[n]['pos'] - system[n-1]['pos']))
            invq2 = invqOptiq(invq1, system[n]['ABCD'])
            x[n] = wpos(invq2)
            w[n] = wsize(invq2)
            a, b, b2 = [], [], []
            for i in frange(system[n]['pos'], system[n+1]['pos'], system[n+1]['pos'] \
                            - system[n]['pos']):
                j = w[n] * sqrt(1 + ((system[0]['lam'] * (i - system[n]['pos'] - x[n])) \
                                / (pi * (w[n]** 2))) ** 2)
                b.append(j)
                b2.append(-j)
                a.append(i)
            if i == fieldpos:

```

## B.2 Shatter system test

```
#!/usr/bin/env python
```

```

import cv
from math import sqrt, pi
import time
import serial

def is_rect_nonzero(r):
    (x, y, w, h) = r
    return (w > 0) and (h > 0)

def contour_iterator(contour):
    while contour:
        yield contour
        contour = contour.h_next()

def closest(target, collection):
    return min(enumerate(collection), key=lambda x: abs(x[1] - target))

class ShatterChecker:

    def __init__(self):
        self.capture = cv.CaptureFromCAM(0)
        cv.NamedWindow("Shatter_Checker", 0)
        cv.SetMouseCallback("Shatter_Checker", self.on_mouse)
        self.drag_start = None      # Set to (x, y) when mouse starts drag
        self.track_window = None    # Set to rect when the mouse drag finishes
        self.onetime = False
        self.fil = open('Shatter_Result.txt', 'w')
        print("Keys:\n"
              "----ESC----quit the program\n"
              "----Click----Reset the selection\n"
              "----To select a region of interest, drag across the frame with the mouse")
        self.serial = serial.Serial(0, 9600, timeout=0.2)
        self.serial.write('P150N')
        time.sleep(0.2)
        self.serial.write('P100N')

        self.serial.close()
        self.run()

    def on_mouse(self, event, x, y, flags, param):
        if event == cv.CV_EVENT_LBUTTONDOWN:
            self.drag_start = (x, y)
        if event == cv.CV_EVENT_LBUTTONUP:
            self.drag_start = None
            self.track_window = self.selection
        if self.drag_start:
            xmin = min(x, self.drag_start[0])
            ymin = min(y, self.drag_start[1])
            xmax = max(x, self.drag_start[0])
            ymax = max(y, self.drag_start[1])
            self.selection = (xmin, ymin, xmax - xmin, ymax - ymin)

    def find_area_circles(self, sub):
        ##      if self.onetime:
        ##          time.sleep(3)
        stor = cv.CreateMemStorage()
        gray = cv.CreateImage(cv.GetSize(sub), 8, 1)
        bw = cv.CreateImage(cv.GetSize(sub), 8, 1)
        cv.CvtColor(sub, gray, cv.CV_BGR2GRAY)
        # Threshold the source image. This needful for cv.FindContours().
        cv.Smooth(gray, gray, cv.CV_GAUSSIAN, 3, 0)
        cv.Threshold(gray, bw, 150, 255, cv.CV_THRESH_BINARY)
        cv.Dilate(bw, bw, None, 2)
        # Find all contours.
        cont = cv.FindContours(bw,
                              stor,
                              cv.CV_RETR_LIST,

```

```

        cv.CV_CHAIN_APPROX_SIMPLE)
self.x, self.area = [], []
for c in contour_iterator(cont):
    moments = cv.Moments(c)
    area = cv.GetCentralMoment(moments, 0, 0)
    x = cv.GetSpatialMoment(moments, 1, 0)/area
    self.x.append(x)
    self.area.append(area)
    # Draw the current contour in blue
    blue = cv.CV_RGB(0, 0, 255)
    cv.DrawContours(self.sub, c, blue, blue, 0, 1, 8, (0, 0))

def run(self):
    while True:
        frame = cv.QueryFrame( self.capture )
        # If mouse is pressed, highlight the current selected rectangle
        if self.drag_start and is_rect_nonzero(self.selection):
            self.sub = cv.GetSubRect(frame, self.selection)
            save = cv.CloneMat(self.sub)
            cv.ConvertScale(frame, frame, 0.5)
            cv.Copy(save, self.sub)
            x,y,w,h = self.selection
            cv.Rectangle(frame, (x,y), (x+w,y+h), (255,255,255))

        # Display ROI selection
        if self.track_window and is_rect_nonzero(self.track_window):
            if not self.onetime:
                self.xref, self.arearef = [], []
                self.find_area_circles(self.sub)
                self.xref = sorted(self.x)
                self.arearef = sorted(self.area)
                cv.ShowImage( "Shatter_Checker", self.sub)
                self.onetime = True
            else :
                self.find_area_circles(self.sub)
                self.state = [ 'Closed ']*len(self.xref)
                for i in xrange(len(self.x)):
                    idx, value = closest(self.x[i], self.xref)
                    self.state[idx] = 'Opened'
                    if abs(self.arearef[idx]-self.area[i])/self.arearef[idx] > 0.2:
                        self.state[idx] = 'Problem'
                now = time.localtime(time.time())
                self.fil.write('Slit'+str(idx)+', had a problem at '\
                               +time.strftime("%H:%M:%S", now)+'\n')
                text = []
                for i in xrange(len(self.xref)):
                    text.append('Slit '+str(i+1)+', '+str(self.state[i]))
                print '\n'.join(text)
                cv.ShowImage( "Shatter_Checker", self.sub)

            else:
                cv.ShowImage( "Shatter_Checker", frame)
                self.onetime = False

            c = cv.WaitKey(7) % 0x100
            if c == 27:
                cv.DestroyWindow("Shatter_Checker")
                break

if __name__=="__main__":
    ShatterChecker()

```

### B.3 Analyze data from measurements

```

from numpy import *
from pylab import *

```

```

#### Data importation and preparation ####

# Data import
f = open('test2.dat', 'r')

# Data preparation
data = [[],[],[],[],[],[],[],[]]
counts = [[],[],[],[],[],[],[],[]]
# First loop to initialise the keys of the dictionary (shatter combinations)
for i in xrange(8):
    line = f.readline()
    data[int(line.split()[0])] = [int(line.split()[1])]
    counts[int(line.split()[0])] = [int(line.split()[1])]
# Second loop to fill the combinations with coincidences
for i in f.readlines():
    data[int(i.split()[0])].append(int(i.split()[1]))
    counts[int(i.split()[0])].append(int(i.split()[1]))
# Now all data are organized by shatter combinaisons
# we can close the file
f.close()

# Putting all of it in numpy arrays
arrays = vstack(array(data[i], dtype=float64) for i in xrange(8))
arrcounts = vstack(array(counts[i], dtype=float64) for i in xrange(8))
arrnorm = (arrcounts - arrays) / mean(arrcounts[0])

# Order them by combination
ind = lexsort((arrays[:,1], arrays[:,0]))
orderarrays = arrays[ind]
orderarrays = orderarrays[::-1]

# Number of points
print len(orderarrays[0])

#### Remove point outside a real deviation of 4 upon a 1000 points set (laser source case)
##def trunc(f, n):
##    '''Truncates/pads a float f to n decimal places without rounding'''
##    slen = len('%.*f' % (n, f))
##    return str(f)[:slen]
##    ## Find how many are complete
##    num = int(trunc((len(data[0]) / 1000), 0)) + 1
##    ## Prepare arrays of the missing values size
##    missing = empty((8,(num) * 1000 - len(data[0]),))
##    ## Fill it with NaN (Not a Number)
##    missing.fill(nan)
##    ## Add them to the arrays
##    arrays = hstack((arrays, missing))
##    arrays = arrays.reshape(8,num,1000)
##    ## Find mean values and standard deviation for each data set
##    means = vstack(hstack(array([mean(arrays[j,i,where(~isnan(arrays[j,i]))],1)]))\
##    ##for i in xrange(num))for j in xrange(8))
##    stds = vstack(hstack(array([std(arrays[j,i,where(~isnan(arrays[j,i]))],1)]))\
##    ##for i in xrange(num))for j in xrange(8))
##    ## Find real deviation and remove points having a deviation of more than 4 over the set
##    dev = vstack(array(hstack(hstack([abs(arrays[j,i,where(~isnan(arrays[j,i]))])\
##    ##means[j][i])/stds[j][i]] for i in xrange(num)))for j in xrange(8)))
##    orderarrays = delete(orderarrays,where(dev>4),1)
##    ##
##    ## Remove too little intensities
##    orderarrays = delete(orderarrays,where(orderarrays[0]<600),1)

# Number of points
print len(orderarrays[0])

# Calculations of epsilon, delta and kappa with errors
eps = lambda x: (x[0] - x[1] - x[2] - x[3] + \
                  x[4] + x[5] + x[6] - x[7])

```

```

delt = lambda x: (abs(x[1] - x[4] - x[5] + x[7]) + \
    abs(x[2] - x[5] - x[6] + x[7]) + \
    abs(x[3] - x[6] - x[4] + x[7]))

kapcc = eps(orderarrays) / delt(orderarrays)

kappacc = mean(kapcc)
errkappacc = std(kapcc) / sqrt(len(kapcc))
kapmcc = eps(mean(orderarrays,1)) / delt(mean(orderarrays,1))

### Plot it
# Data intensity plot (coincidences in cps)
figure(1)

subplot(1,2,1)
for i in xrange(8):
    plot(orderarrays[i], 'o')
xlabel('Points for every shatter combination')
ylabel('Intensity (number of counts)')

subplot(1,2,2)
plot(kapcc)
axhline(y=kappacc, color='red')
axhline(y=kapmcc, color='green')
ylabel('Kappa values')

suptitle('mean_of_k'+str(abs(mean(kappacc)))+'_std'+str(mean(errkappacc)) + '_red_line') + \
'\n'+ 'k_of_mean'+str(abs(kapmcc)) + '_green_line')

# Peres criterion
criterion = lambda x,y,z: ((x-y-z)/(2*sqrt(y*z)))
alpha = criterion(orderarrays[1], orderarrays[4], orderarrays[5])
beta = criterion(orderarrays[3], orderarrays[5], orderarrays[6])
gamma = criterion(orderarrays[2], orderarrays[4], orderarrays[6])
F = alpha**2 + beta**2 + gamma**2 - abs(2*alpha*beta*gamma)

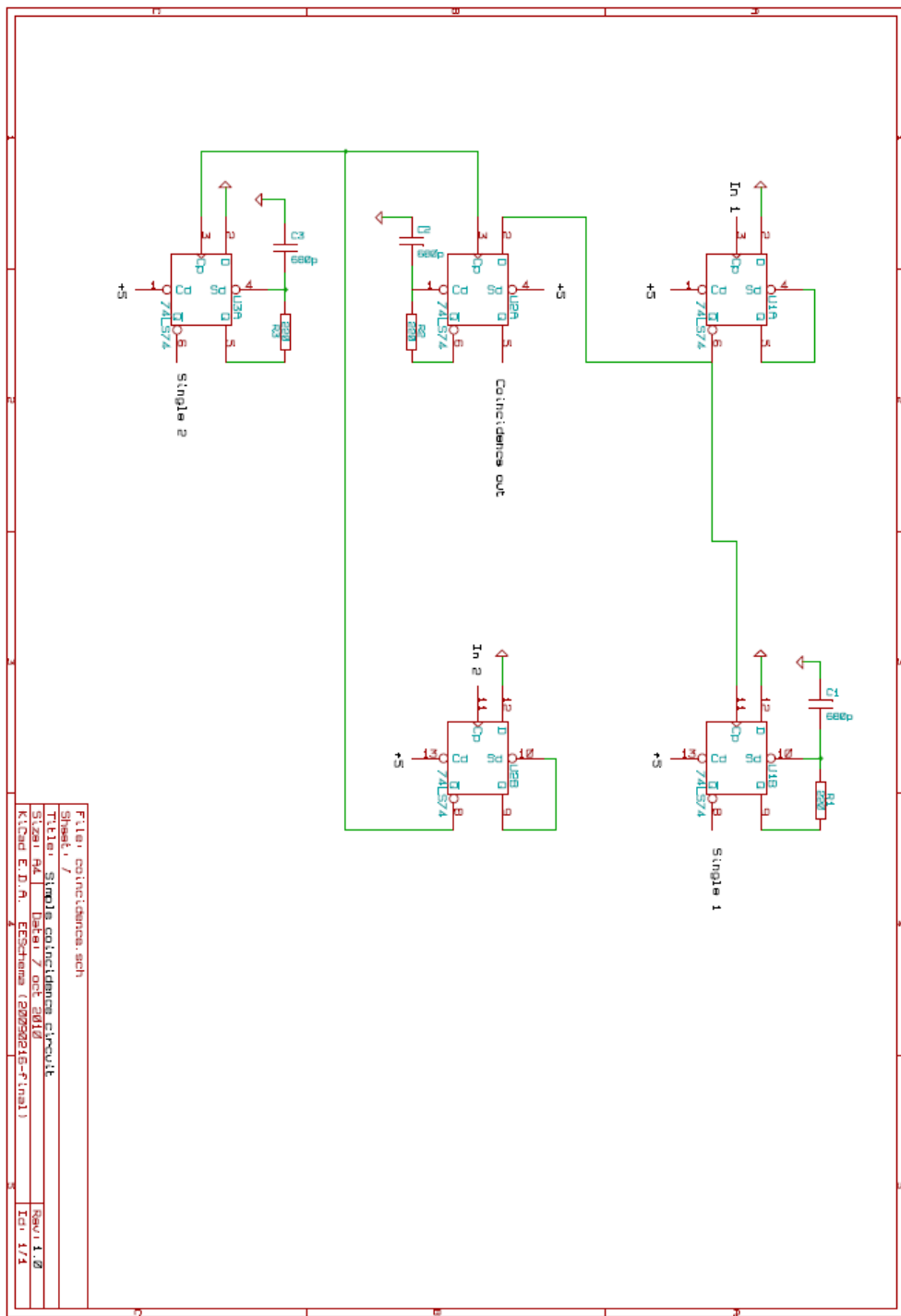
print mean(F)

show()

```

## C Electronics schematics

### C.1 Coincidence circuit



## C.2 Stepper motors driver circuit

